

BUDAPEST UNIVERSITY OF TECHNOLOGY AND ECONOMICS
FACULTY OF MECHANICAL ENGINEERING
DEPARTMENT OF APPLIED MECHANICS

DÁVID HERCZEG
TDK Research

Stability analysis of turning processes with constant and variable
spindle speed

Supervisor:

Dr. Dániel Bachrathy

associate professor

MTA-BME Lendület Machine Tool Vibration Research Group

Department of Applied Mechanics, Budapest University of

Technology and Economics, Budapest H-1521, Hungary

BUDAPEST, 2023

Contents

- 1 Introduction** **1**

- 2 Analytical stability testing** **2**
 - 2.1 Mechanical model 2
 - 2.2 Solution in time domain 3
 - 2.3 Solution in frequency domain 9

- 3 Numerical stability testing** **12**
 - 3.1 Implicit subspace iteration method 12
 - 3.2 Constant spindle speed 15
 - 3.3 Spindle speed variation 20
 - 3.4 Spindle speed function optimization 23

- 4 Stability testing with measurements** **25**
 - 4.1 Cutting force characteristic 25
 - 4.1.1 Measurement 25
 - 4.2 Dynamic properties of the system 32
 - 4.2.1 Measurement 32
 - 4.3 Stability testing 37
 - 4.3.1 Measurement setup 37
 - 4.3.2 Constant spindle speed 38
 - 4.3.3 Periodic spindle speed (SSV) 39

- 5 Summary** **41**

- Reference** **43**

1 Introduction

In the manufacturing industry, there is an ongoing quest for enhancing efficiency, precision and cost-effectiveness throughout the manufacturing process. To accomplish this objective, a series of advanced mathematical models had been developed to gain a deeper insight into tool vibrations. Not only can these unwanted high-amplitude vibrations known as 'chatter', substantially impact surface quality of the product, but it also has the potential to initiate tool breakages, which can cascade into formidable challenges for manufacturers, leading to downtime and financial losses for the company. This has been a challenge fascinating many engineers since the early 20th century and continues to be a widely studied and researched field [1]. Depending on the mechanical model used, there are numerical and sometimes analytical solutions available to determine the so-called stability map, which is a useful tool to identify whether we can expect the phenomenon of chatter [2]. The concept of varying the spindle speed arises from the necessity of finding a solution to expand the stable region in the stability map around a given spindle speed and feed rate [3].

The main objective of this work is to present the stability analysis of both constant speed turning and the variable speed turning solution, placing a greater emphasis on examining the periodic variation of the spindle speed. This will be achieved by carrying out analytical and numerical analysis for stability testing. We will measure the input data required for the calculations, such as the dynamic properties of the system through modal analysis and the cutting force characteristic with the help of the force sensor found in the Department of Applied Mechanics at BME. The varying spindle speed is generated using a frequency inverter, which allows us to demonstrate the effects of the frequency and amplitude of the spindle speed variation on the stability of the system.

2 Analytical stability testing

2.1 Mechanical model

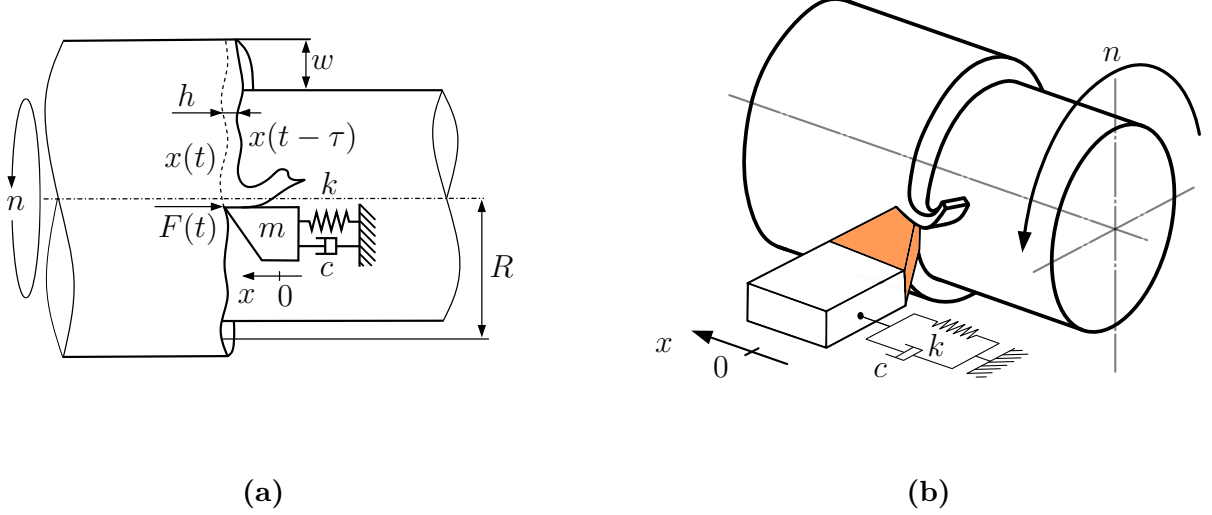


Figure 2.1: Mechanical model, (a) 2D view, (b) 3D view

In a single-degree-of-freedom model, we observe the lateral deflection of the tool in the x -direction relative to the workpiece. The occurrence of the tool vibration can be initiated from the imperfection of the workpiece surface or any external disturbances. Using Newtons II. law of motion and the following notations: m for mass, k for stiffness, c for damping, and the tool position is x , the equation of motion looks as follow:

$$m\ddot{x} + c\dot{x} + kx = F(t). \quad (2.1)$$

where the excitation force $F(t)$ can be determined by the force characteristic of the tool. In practice, various models exist for the relationship between the cutting force and the size of the chip to be separated. In our case, we introduce a shifted linear characteristics:

$$F_c(h, w) = F_0 + K_1 w(K_0 + h). \quad (2.2)$$

When substituted into the equation of motion, taking into account its direction illustrated in Fig. 2.1a it looks as

$$F(t) = -F_c(h, w), \quad (2.3)$$

$$F(t) = -F_0 - K_1 w(K_0 + h(t)). \quad (2.4)$$

We can see that the force acting on the tool in the x -direction is proportional to the cutting coefficients K_0 and K_1 , the depth of cut w (also known as the chip width) and the chip thickness $h(t)$. We also consider a shift in the cutting force with a constant F_0 for a better fitting to the measured data. However, since the chip thickness to be removed at

a given moment depends on the current tool position and the one revolution earlier, the excitation force can be formulated with a delayed term. The actual chip thickness $h(t)$ can be expressed (according to Fig. 2.1a) in the function of the nominal chip thickness h_0 , the actual position of the tool $x(t)$, and the position of the tool one revolution earlier $x(t - \tau)$

$$h(t) = h_0 + x(t) - x(t - \tau). \quad (2.5)$$

where τ is the time delay, which is the time period of the lathe's spindle with the spindle speed of Ω in [rad/s]. When using a constant spindle speed τ is also a constant which can be expressed as

$$\tau = \frac{2\pi}{\Omega}. \quad (2.6)$$

Thus the equation of motion can be formulated in the following way, after substituting Eq. (2.4) and Eq. (2.5) into Eq. (2.1)

$$m\ddot{x} + c\dot{x} + kx = -F_0 - K_1w(K_0 + h_0 + x(t) - x(t - \tau)). \quad (2.7)$$

Normalizing it with the mass we get

$$\ddot{x} + \frac{c}{m}\dot{x} + \frac{k}{m}x = -\frac{F_0}{m} - \frac{K_1w}{m}(K_0 + h_0 + x(t) - x(t - \tau)). \quad (2.8)$$

Introducing the dimensionless machining coefficient φ for later convenience

$$\varphi = \frac{K_1w}{k} \quad (2.9)$$

and substituting the parameters with the modal parameters, where ω_n is the natural frequency and ζ is the damping factor, we get the following second-order delayed differential equation (DDE).

$$\ddot{x} + 2\zeta\omega_n\dot{x} + \omega_n^2x = -\omega_n^2x_{st} - \omega_n^2\varphi(x(t) - x(t - \tau)). \quad (2.10)$$

Where the static deformation of the tool is

$$x_{st} = \frac{F_0 + K_1K_0w + K_1wh_0}{k}. \quad (2.11)$$

In the following subsections, we discuss the solutions of this differential equation in time and frequency domain. The main goal is to determine the stability boundary of the system in the function of Ω and w machining parameters.

2.2 Solution in time domain

Since the solution to second-order ODEs is well known, here we also seek the solution in a similar trial function form, but first for more convenience let's transform the equation of

motion with a new coordinate $y(t)$, by shifting the solution with a constant value which is the static deformation of the tool.

$$y(t) = x(t) + x_{st}. \quad (2.12)$$

Now the transformed equation of motion looks as follows

$$\ddot{y} + 2\zeta\omega_n\dot{y} + \omega_n^2 y = \omega_n^2 \varphi(y(t - \tau) - y(t)). \quad (2.13)$$

As mentioned earlier, we seek the solution in a similar form to that of second-order ODEs, which is an exponential trial function

$$y(t) = Ae^{\lambda t}. \quad (2.14)$$

Substituting this into Eq. (2.13)

$$A\lambda^2 e^{\lambda t} + 2\zeta\omega_n A\lambda e^{\lambda t} + \omega_n^2 A e^{\lambda t} = \omega_n^2 \varphi(Ae^{\lambda(t-\tau)} - Ae^{\lambda t}). \quad (2.15)$$

After some simplification we get

$$Ae^{\lambda t}(\lambda^2 + 2\zeta\omega_n\lambda + \omega_n^2 - \omega_n^2\varphi e^{-\lambda\tau} + \omega_n^2\varphi) = 0. \quad (2.16)$$

To obtain a non-trivial solution ($A \neq 0$), the terms within parentheses must be equal to zero

$$\lambda^2 + 2\zeta\omega_n\lambda + \omega_n^2 - \omega_n^2\varphi e^{-\lambda\tau} + \omega_n^2\varphi = 0. \quad (2.17)$$

We look for the λ exponent in a complex form, like

$$\lambda = \sigma + \omega i. \quad (2.18)$$

Substituting the previous equation into Eq. (2.17) we get

$$(\sigma + \omega i)^2 + 2\zeta\omega_n(\sigma + \omega i) + \omega_n^2 - \omega_n^2\varphi e^{-(\sigma + \omega i)\tau} + \omega_n^2\varphi = 0. \quad (2.19)$$

However, if we are only concerned with the stability boundary, disregarding the fact that it may not always be advantageous from an engineering perspective, we seek the solution in a form where

$$\sigma = 0. \quad (2.20)$$

Which means, that the amplitude of the vibration remains constant in time.

After the substitution, and applying Euler's formula for the term with the imaginary exponent

$$e^{-i\omega\tau} = \cos(-\omega\tau) + i \sin(-\omega\tau). \quad (2.21)$$

We get the following equation which is called the characteristic equation

$$D(i\omega) = -\omega^2 + 2\zeta\omega_n\omega i + \omega_n^2 - \omega_n^2\varphi \cos(\omega\tau) + \omega_n^2\varphi \sin(\omega\tau)i + \omega_n^2\varphi = 0. \quad (2.22)$$

The characteristic equation can only be satisfied if the real and imaginary parts are both equal to zero

$$\text{Re}(D(i\omega)) = -\omega^2 + \omega_n^2 + \omega_n^2\varphi - \omega_n^2\varphi \cos(\omega\tau) = 0, \quad (2.23)$$

$$\text{Im}(D(i\omega)) = 2\zeta\omega_n\omega + \omega_n^2\varphi \sin(\omega\tau) = 0. \quad (2.24)$$

Now the goal is to find those pairs of Ω and w for which the system of equations is satisfied. Remember that from Eq. (2.9) and Eq. (2.6) the φ is the function of w and τ is the function of Ω . This way by finding these $\tau - \varphi$ pairs, we can also find the $\Omega - w$ pairs. After solving the system of equations for φ and τ we get

$$\varphi = \frac{1}{2\omega_n^2} \frac{4\zeta^2\omega_n^2\omega^2 + (\omega_n^2 - \omega^2)^2}{\omega^2 - \omega_n^2}, \quad (2.25)$$

$$\tau = \frac{2}{\omega} \arctan\left(\frac{\omega_n^2 - \omega^2}{2\zeta\omega_n\omega}\right) + \frac{2j\pi}{\omega} \quad j = 1, 2, 3, \dots \quad (2.26)$$

We can express w and Ω in the function of ω in the following way:

$$w(\omega) = \frac{m}{2K_1} \frac{4\zeta^2\omega_n^2\omega^2 + (\omega_n^2 - \omega^2)^2}{\omega^2 - \omega_n^2}, \quad (2.27)$$

$$\Omega(\omega) = \frac{\pi\omega}{\arctan\left(\frac{\omega_n^2 - \omega^2}{2\zeta\omega_n\omega}\right) + j\pi}, \quad j = 1, 2, 3, \dots \quad (2.28)$$

These $\Omega - w$ pairs determine the curves what are known as 'lobes,' which mark the points where the roots of the characteristic equation are purely complex. These are also commonly referred to as transition curves. These transition curves separate the plane into regions where the number of unstable characteristic roots is constant. With preliminary parameters shown in Table 2.1 the stability map looks like

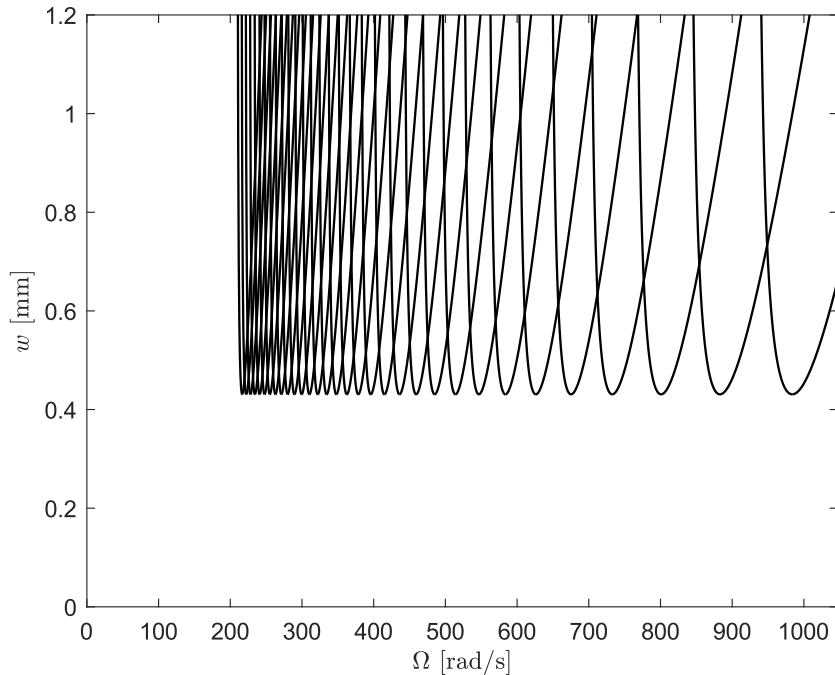


Figure 2.2: Stability lobes the with preliminary parameters seen in Tab. 2.1

Parameter	Value	Dimension
m	0.1	kg
k	$7 \cdot 10^6$	N/m
c	50	Ns/m
K_1	10^9	N/m^2

Table 2.1: Preliminary parameters

Stable domains associated with zero unstable characteristic roots, which are the domains below the lower envelope of the lobes. The number of unstable roots in different domains can be expressed using the Stepan formulas. However, in machining, any region containing unstable roots should be avoided. Therefore, the region of interest is the area below the lower envelope. This can be constructed by finding the intersection points of adjacent lobes and by plotting the portion of the curve which is below these intersections shown in Fig. 2.3a. A more practical use of this map is to plot the spindle speed specified in RPM (Revolutions Per Minute) shown in Fig. 2.3b, which can be calculated as

$$n = 60 \frac{\Omega}{2\pi}. \quad (2.29)$$

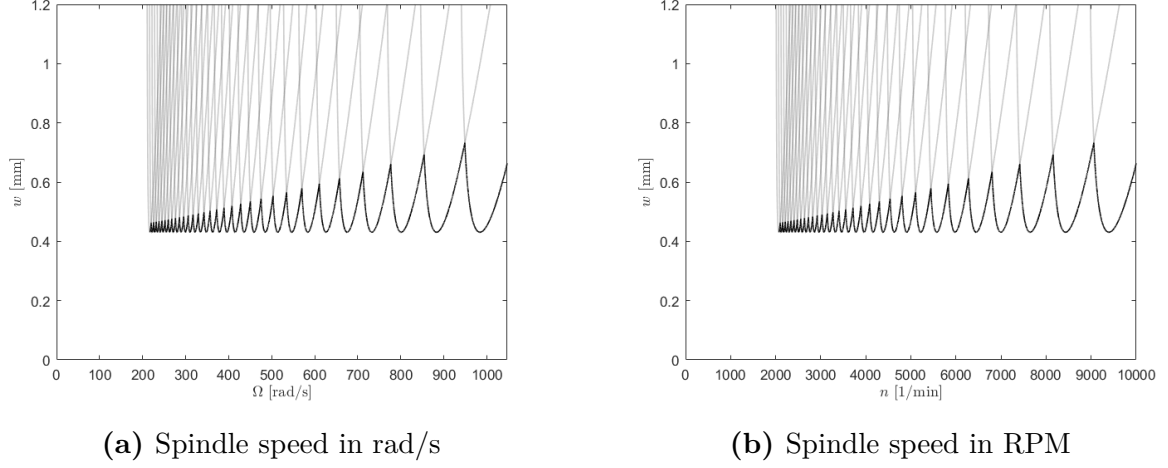


Figure 2.3: Stability map with lower envelope curves highlighted

Each of these lobes correspond to a different j value, as deduced from Eq. (2.28). The higher the value of j , the more the lobes shift towards the left side. It is important to mention that each lobe reaches the same minimum w value, which can be easily proven by taking the derivative of $w(\omega)$ with respect to ω and find the local minimum points.

$$\frac{dw}{d\omega} = \frac{m}{2K_1} \frac{(8\zeta^2\omega_n^2\omega - 4\omega(\omega_n^2 - \omega^2))(\omega^2 - \omega_n^2) - 2\omega(4\zeta^2\omega_n^2\omega^2 + (\omega_n^2 - \omega^2)^2)}{(\omega^2 - \omega_n^2)^2}. \quad (2.30)$$

The extremum of $w(\omega)$ can be where the derivative is zero, this can only be fulfilled when the numerator in Eq. (2.30) is zero, thus

$$(8\zeta^2\omega_n^2\omega - 4\omega(\omega_n^2 - \omega^2))(\omega^2 - \omega_n^2) - 2\omega(4\zeta^2\omega_n^2\omega^2 + (\omega_n^2 - \omega^2)^2) = 0. \quad (2.31)$$

After solving the equation above, there are 4 roots for the equation.

$$\omega = \pm\omega_n\sqrt{1 \pm 2\zeta}. \quad (2.32)$$

Yet our interest lies in the positive roots, let's call them $\hat{\omega}$

$$\hat{\omega} = \omega_n\sqrt{1 \pm 2\zeta}. \quad (2.33)$$

Which we can substitute into $w(\omega)$

$$w(\hat{\omega}) = \frac{m}{2K_1} \frac{4\zeta^2\omega_n^2(\omega_n\sqrt{1 \pm 2\zeta})^2 + (\omega_n^2 - (\omega_n\sqrt{1 \pm 2\zeta})^2)^2}{\omega_n^2 - (\omega_n\sqrt{1 \pm 2\zeta})^2}. \quad (2.34)$$

Which equation simplifies to the following equation, where \hat{w} denotes the minimum positive w values

$$\hat{w} = 2\frac{m}{K}\zeta\omega_n^2(1 + \zeta). \quad (2.35)$$

So we have proven that the minimum of each lobe takes the same value of w . In research, it is common to express the quantities in their dimensionless form. To achieve this, we

use the following method to remove the dimensions, where \tilde{w} and $\tilde{\Omega}$ are the dimensionless chip width and spindle speed.

$$\tilde{w} = \frac{wK_1}{k}, \quad (2.36)$$

$$\tilde{\Omega} = \frac{\Omega}{\omega_n}. \quad (2.37)$$

Using the new formulas above, the dimensionless feed rate and the dimensionless spindle speed are

$$\tilde{w}(\omega) = \frac{m}{wk} \frac{4\zeta^2\omega_n^2\omega^2 + (\omega_n^2 - \omega)^2}{\omega^2 - \omega_n^2}, \quad (2.38)$$

$$\tilde{\Omega}(\omega) = \frac{1}{\omega_n} \frac{\pi\omega}{\arctan\left(\frac{\omega_n^2 - \omega^2}{2\zeta\omega_n\omega}\right) + j\pi}, \quad j = 1, 2, 3, \dots \quad (2.39)$$

Which is also presented in Fig. 2.4.

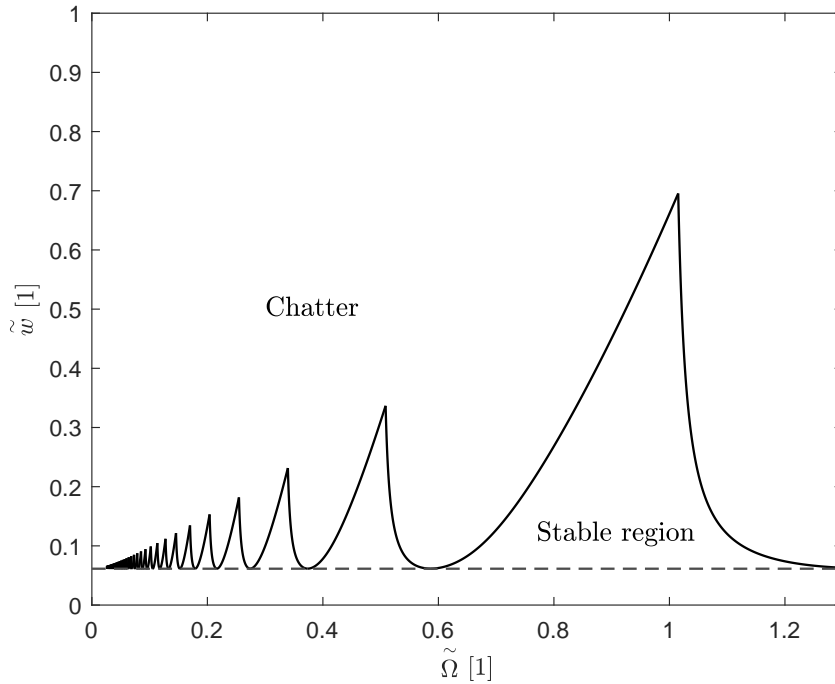


Figure 2.4: Dimensionless stability map, where black lines denote the stability boundary and the dashed line is the lower envelope of the curves

Based on the equations, we could see that the position of these lobes greatly depend on the modal parameters, primarily the damping factor, where even a slight change results in significant modifications. The effect of the damping factor on the lobes can be seen in Fig. 2.5.

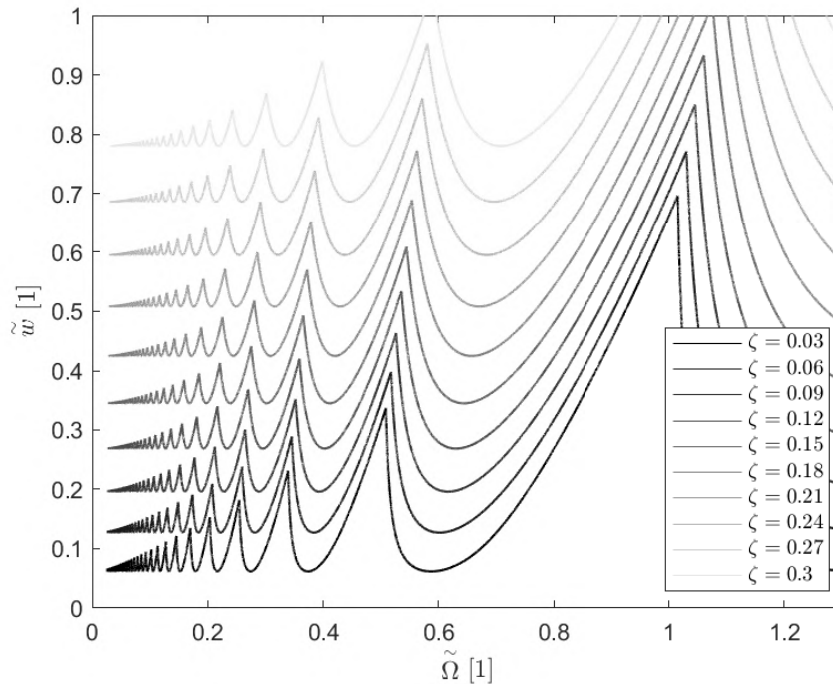


Figure 2.5: Effect of damping factor on the stability map

2.3 Solution in frequency domain

While time-domain approach is widely used when solving differential equations, the frequency domain solution offers an alternative perspective. In this approach we analyze the behaviour of the system as a function of frequency rather than time. It can be advantageous when dealing with systems excited by periodic or harmonic load, as we can gain sight into the system's response to different frequency components.

The Fourier transform is an essential tool to analyze the frequency domain solution. The general formula of the Fourier transform is

$$\mathcal{F}\{x(t)\} = \int_{-\infty}^{\infty} x(t)e^{-i\omega t} dt. \quad (2.40)$$

For a reminder the transformation rules when transforming the sum of two functions, is just the sum of the transform of the functions individually

$$\mathcal{F}\{x(t) + y(t)\} = X(\omega) + Y(\omega). \quad (2.41)$$

When transforming the derivative of a function, it appears to be a multiplication in the frequency domain

$$\mathcal{F}\{\dot{x}(t)\} = i\omega X(\omega), \quad (2.42)$$

and last but not least, the transform of a delayed function is

$$\mathcal{F}\{x(t - \tau)\} = X(\omega)e^{-i\omega\tau}. \quad (2.43)$$

In our example the motion equation is

$$m\ddot{x}(t) + c\dot{x}(t) + kx(t) = F(t). \quad (2.44)$$

Using the following notations for the Fourier transform of $x(t)$ and $F(t)$.

$$x(t) \xrightarrow{\text{Fourier transform}} X(\omega) \quad (2.45)$$

$$F(t) \xrightarrow{\text{Fourier transform}} \Phi(\omega) \quad (2.46)$$

The transformed equation according to the above mentioned transformation rules is

$$-\omega^2 mX(\omega) + i\omega X(\omega) + kX(\omega) = \Phi(\omega). \quad (2.47)$$

Afterward, the transfer function $H(i\omega)$ can be derived, which provides the system's response signals for a given frequency excitation:

$$H(\omega) = \frac{X(\omega)}{\Phi(\omega)}. \quad (2.48)$$

After rearranging Eq. (2.47), will give us the transfer function in the form of

$$H(\omega) = \frac{1}{-\omega^2 m + i\omega c + k}. \quad (2.49)$$

Also this means that according to Eq. (2.48) $X(\omega)$ can be expressed as

$$X(\omega) = H(\omega)\Phi(\omega). \quad (2.50)$$

To get to the same outcome, like in Eq. (2.22), it is necessary to examine $\Phi(\omega)$ further. As we know from Eq. (2.7), according to the mechanical model

$$F(t) = -F_0 - K_1 w(K_0 + h_0 + x(t) - x(t - \tau)). \quad (2.51)$$

Transforming the equation above while neglecting the static terms, since they serve as a constant shift in the solution and analysing only $y(t)$, will give us

$$\Phi(\omega) = Y(\omega)K_1 w(e^{-i\omega\tau} - 1). \quad (2.52)$$

Substituting this into Eq. (2.48):

$$Y(\omega) = H(\omega)Y(\omega)K_1 w(e^{-i\omega\tau} - 1). \quad (2.53)$$

Rearranging the equation above will result

$$Y(\omega)(H(\omega)K_1 w(e^{-i\omega\tau} - 1) - 1) = 0. \quad (2.54)$$

We are looking for a solution where the $Y(\omega)$ term is not zero. So our equation satisfies when

$$H(\omega)K_1 w(e^{-i\omega\tau} - 1) - 1 = 0. \quad (2.55)$$

This step is analogous to when we were looking for its non-trivial solution in the time domain in Eq. (2.16). The real and the imaginary part of the above equation can be used directly in the Multi-Dimensional Bisection Method (MDBM) [4] to find the stability lobes numerically based on the directly measured transfer function. This method is applied later in the experiments to check the validity of the fitted analytical models. Substituting the $H(\omega)$ and rearranging the equation, we get to a simplified form:

$$-\omega^2 + \frac{i\omega c}{m} + \frac{k}{m} - \frac{K_1 w}{m}(e^{-i\omega\tau} - 1) = 0. \quad (2.56)$$

Using the modal parameters we arrive at the following characteristic equation, whose solution is entirely equivalent of Eq. (2.22).

$$-\omega^2 + 2\zeta\omega_n\omega i + \omega_n^2 - \omega_n^2\varphi \cos(\omega\tau) + \omega_n^2\varphi \sin(\omega\tau)i + \omega_n^2\varphi = 0. \quad (2.57)$$

From this point, the derivation of the stability boundary is exactly the same as in the time-domain case, as detailed in the previous subsection earlier after Eq. (2.22).

3 Numerical stability testing

The above-mentioned methods can be used for constant spindle speed turnings. For the spindle speed variation, it is necessary to use a different method. A well-known method for such a periodic system is the Multi-Frequency Method [5] in frequency domain. In the time domain one of the widely used method is the semi-discretization method [6] or the Implicit Subspace Iteration Method [7]

3.1 Implicit subspace iteration method

Prior to introducing the ISIM for stability analysis, it is crucial to commence with the foundational method known as the semi-discretization method (SDM). This method serves as a fundamental and efficient approach for stability analysis. In semi-discretization a linear mapping can be defined between two states corresponding to two neighbouring time steps in a way like

$$\mathbf{z}_{i+1} = \mathbf{G}_i \mathbf{z}_i. \quad (3.1)$$

Where \mathbf{G}_i denotes the coefficient matrix connecting the two states \mathbf{z}_i and \mathbf{z}_{i+1} , which are the vectors of the discretized states sampled of the continuous state-space of the delayed interval at the discrete time intervals at subsequent time instants. In our case, the \mathbf{z}_i vectors contain the position and the velocity of the tool, thereby describing the system's state at the given moment.

If these linear mappings are changed by simple multiplications over the time-periodicity, a discrete map can be defined between the initial delay-discrete state \mathbf{z}_0 and the state \mathbf{z}_τ with one period later:

$$\mathbf{z}_\tau = \mathbf{G}_n \dots \mathbf{G}_2 \mathbf{G}_1 \mathbf{G}_0 \mathbf{z}_0 = \mathbf{\Phi} \mathbf{z}_0. \quad (3.2)$$

where $\mathbf{\Phi}$ is the transition matrix, a finite approximation of the infinite dimensional monodromy operator. This way the stability analysis is reduced to a problem where we have to find whether absolute values of all the eigenvalues of $\mathbf{\Phi}$ are less than one:

$$|\mu_i| < 1. \quad (3.3)$$

To construct the whole $\mathbf{\Phi}$ matrix, the SDM method uses the above-mentioned matrix multiplication with some further approximation. To determine the \mathbf{z}_T vector for different initial conditions we used a 4th order Runge-Kutta method (RK4). This can be rewritten in a form where we collect all the \mathbf{z}_0 and \mathbf{z}_T vectors in the columns of \mathbf{Z}_0 and \mathbf{Z}_T matrices:

$$\mathbf{Z}_T = \mathbf{\Phi} \mathbf{Z}_0. \quad (3.4)$$

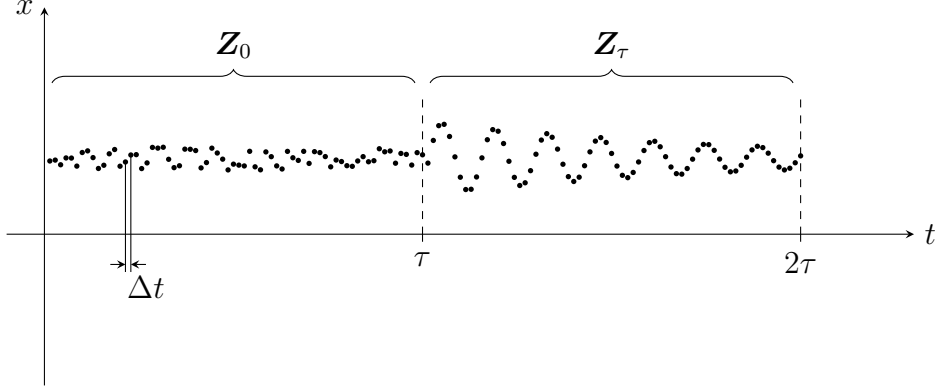


Figure 3.1: The graphical illustration of the semi-discretization method

If we choose the \mathbf{Z}_0 matrix to be the identity matrix, the problem significantly simplifies, because in this case

$$\mathbf{Z}_T = \Phi. \quad (3.5)$$

In order to check the stability criteria in Eq. (3.3), we only have to find the eigenvalue of Φ with the largest absolute value and check that its magnitude is less than one, because in such cases, the absolute value of all the other eigenvalues are smaller than one.

$$|\mu_n| < \dots < |\mu_2| < |\mu_1| < 1. \quad (3.6)$$

With the ISIM [7], it is possible to determine the stability without calculating the whole Φ matrix. To better understand this method, consider the general eigenvalue problem

$$\Phi \mathbf{S} = \mathbf{S} \boldsymbol{\mu}. \quad (3.7)$$

Φ being an $n \times n$ square matrix, $\boldsymbol{\mu}$ is a diagonal matrix of size $n \times n$ of the eigenvalues of Φ and \mathbf{S} of size $n \times n$ containing the eigenvectors of Φ in its columns. The first N_s eigenvalues of the largest absolute value can be iteratively determined ($N_s < n$). Let us assume that \mathbf{S}_j is an $n \times N_s$ size matrix of the first N_s approximated dominant eigenvectors of Φ in its columns, after the j^{th} iteration step. With the following operation the new set of \mathbf{V}_j with size of $n \times N_s$ can be calculated

$$\mathbf{V}_j = \Phi \mathbf{S}_j. \quad (3.8)$$

After sufficient iteration steps, \mathbf{S}_j will converge to the dominant eigenvectors and the basis formed by the column vectors in both \mathbf{S}_j and \mathbf{V}_j span approximately the same space. Therefore, an approximate matrix \mathbf{H}_j of size $N_s \times N_s$ connecting \mathbf{S}_j and \mathbf{V}_j can be obtained using a pseudo-inverse calculation from the relation

$$\mathbf{V}_j \approx \mathbf{S}_j \mathbf{H}_j \quad (3.9)$$

↓

$$\mathbf{H}_j = (\mathbf{S}_j^T \mathbf{S}_j)^{-1} \mathbf{S}_j^T \mathbf{V}_j. \quad (3.10)$$

where matrix \mathbf{H}_j represents a subspace of size $N_s \times N_s$ of the original space of matrix Φ of size $n \times n$. After several iteration steps, the eigenvalues of \mathbf{H}_j provide a good approximation for the dominant eigenvalues of Φ . This way, it is enough to compute the eigenvalues of a significantly reduced $N_s \times N_s$ sized matrix \mathbf{H}_j instead of the large $n \times n$ sized matrix Φ .

In the case of a known matrix Φ , the iteration can be initiated from a random array of \mathbf{S}_0 , and Eq. (3.8) and Eq. (3.10) can be used to calculate the approximation of the dominant eigenvectors after one iteration step. Normalizing the result:

$$\mathbf{S}_{j+1} = \mathbf{V}_j \mathbf{A}_j, \quad (3.11)$$

where \mathbf{A}_j is a matrix containing the eigenvectors of \mathbf{H}_j , the same formula can be applied again and again until convergence of the dominant eigenvectors is achieved.

The sizes of the previously mentioned \mathbf{Z}_0 and \mathbf{Z}_T matrices depend on the resolution of the time Δt . Therefore if

$$n = \frac{\tau}{\Delta t} \quad (3.12)$$

it implies that \mathbf{Z}_0 , \mathbf{Z}_T and Φ are sizes of $2n \times 2n$. As we seen in Eq. (2.6) a lower spindle speed leads to a higher τ which leads to a greater size matrix. Despite the fact that with the iteration seen in Eq. (3.10) it is available to determine the largest absolute value eigenvalue of a larger matrix of Φ , the challenge of acquiring the complete Φ matrix in a short time remains. This is where the ISIM proves to be advantageous, because it is also possible to determine the matrix \mathbf{H}_j without calculating the whole Φ matrix, only the mapping of \mathbf{S}_j to \mathbf{V}_j is needed, which can be performed by numerical RK simulation. The vectors in the columns of \mathbf{V}_j can be calculated directly from the equation of motion of the system. With the combination of ISIM and the SDM the iteration looks as follow

$$\begin{aligned} \mathbf{S}_j &\xrightarrow{\text{Time integration}} \mathbf{V}_j \\ \mathbf{H}_j &= (\mathbf{S}_j^T \mathbf{S}_j)^{-1} \mathbf{S}_j^T \mathbf{V}_j \\ \mathbf{S}_{j+1} &= \mathbf{V}_j \mathbf{A}_j \boldsymbol{\mu}_j^{-1}, \end{aligned} \quad (3.13)$$

where the interaction is starting from a random \mathbf{S}_0 . Note that a normalization has been included using the eigenvalues of \mathbf{H}_j in the diagonals of $\boldsymbol{\mu}_j$ at the final step of each iteration. This step aims to mitigate the potential numerical errors that may appear if the values in matrix \mathbf{S} increase rapidly.

3.2 Constant spindle speed

In order to generate the stability map of machining with a Constant Spindle Speed (CSS) using the ISIM we need a numerical solver, that finds the solutions of the equation of motion for a given set of initial conditions. To accomplish this take a look again at the equation of motion seen in Eq. (2.10)

$$\ddot{x} + 2\zeta\omega_n\dot{x} + \omega_n^2x = -\omega_n^2x_{st} - \omega_n^2\varphi(x(t) - x(t - \tau)). \quad (3.14)$$

For this DDE the simplest and one of the most reliable solver is a 4th-order Runge-Kutta method, which requires a transformation of the second-order DDE to a first order system of differential equations. This conversion can be achieved by reformulating Eq. (3.14) with the Cauchy transform, thereby introducing the new coordinates:

$$\boldsymbol{\psi} \equiv \begin{bmatrix} \psi_1 \\ \psi_2 \end{bmatrix} = \begin{bmatrix} x \\ \dot{x} \end{bmatrix}. \quad (3.15)$$

And according to the Cauchy transformation Eq. (3.14) can be reformulated as

$$\dot{\boldsymbol{\psi}} = \mathbf{f}(\boldsymbol{\psi}, t). \quad (3.16)$$

Which means the derivative of the new coordinates are

$$\dot{\boldsymbol{\psi}} = \begin{bmatrix} \dot{\psi}_1 \\ \dot{\psi}_2 \end{bmatrix} = \begin{bmatrix} \psi_2(t) \\ \omega_n^2\varphi\psi_1(t - \tau) - \omega_n^2x_{st} - 2\zeta\omega_n\psi_2(t) - (\omega_n^2 + \omega_n^2\varphi)\psi_1(t) \end{bmatrix}. \quad (3.17)$$

Now that we have our system of 1th order differential equations (note, that $\psi_1(t - \tau)$ is treated as an external excitation known by the previous values of the simulation), we can apply the Runge-Kutta method, which is briefly demonstrated. Suppose we are given an ordinary differential equation with initial conditions below:

$$\dot{y} = f(y, t), \quad (3.18)$$

$$y(t_0) = y_0. \quad (3.19)$$

According to the numerical method, the $(i + 1)^{th}$ term of the solution is

$$y_{i+1} = y_i + \frac{h}{6}(k_1 + 2k_2 + 2k_3 + k_4). \quad (3.20)$$

At the time of

$$t_{i+1} = t_i + \Delta t. \quad (3.21)$$

At the time of Δt , where the k_j values are:

$$\begin{aligned} k_1 &= f(t_i, y_i), \\ k_2 &= f\left(t_i + \frac{\Delta t}{2}, y_i + \Delta t \frac{k_1}{2}\right), \\ k_3 &= f\left(t_i + \frac{\Delta t}{2}, y_i + \Delta t \frac{k_2}{2}\right), \\ k_4 &= f(t_i + \Delta t, y_i + \Delta t k_3). \end{aligned} \quad (3.22)$$

This method can be expanded to a system of ODEs. By reformulating Eq. (3.17), we get the following equation

$$\begin{bmatrix} \psi_{1,i+1} \\ \psi_{2,i+1} \end{bmatrix} = \begin{bmatrix} \psi_{1,i} \\ \psi_{2,i} \end{bmatrix} + \frac{h}{6} \begin{bmatrix} k_1^{\psi_1} + 2k_2^{\psi_1} + 2k_3^{\psi_1} + k_4^{\psi_1} \\ k_1^{\psi_2} + 2k_2^{\psi_2} + 2k_3^{\psi_2} + k_4^{\psi_2} \end{bmatrix}. \quad (3.23)$$

Where the upper indices ψ_1 and ψ_2 are indicating which coordinate the given k_i term corresponds to. We can obtain a more programmable form by rewriting the equation above to

$$\begin{aligned} t_{i+1} &= t_i + \Delta t, \\ \boldsymbol{\psi}_{i+1} &= \boldsymbol{\psi}_i + \frac{\Delta t}{6} (\mathbf{k}_1 + 2\mathbf{k}_2 + 2\mathbf{k}_3 + \mathbf{k}_4), \\ \mathbf{k}_1 &= \mathbf{f}(t_i, \psi_1, \psi_2), \\ \mathbf{k}_2 &= \mathbf{f}\left(t_i + \frac{\Delta t}{2}, \psi_i + \frac{\Delta t}{2} \mathbf{k}_1\right), \\ \mathbf{k}_3 &= \mathbf{f}\left(t_i + \frac{\Delta t}{2}, \psi_i + \frac{\Delta t}{2} \mathbf{k}_2\right), \\ \mathbf{k}_4 &= \mathbf{f}(t_i + \Delta t, \boldsymbol{\psi}_i + \Delta t \mathbf{k}_3). \end{aligned} \quad (3.24)$$

Where the vector \mathbf{f} looks as

$$\mathbf{f} = \begin{bmatrix} \psi_2 \\ \omega_n^2 \varphi \psi_1(t - \tau) - \omega_n^2 x_{st} - 2\zeta \omega_n \psi_2 - (\omega_n^2 + \omega_n^2 \varphi) \psi_1 \end{bmatrix}. \quad (3.25)$$

However, since \mathbf{f} contains a delayed term, $\psi_1(t - \tau)$, it means that we need a ψ_1 value which was taken τ time earlier. If τ is a multiple of Δt time step, then it can be written like

$$\tau = l \cdot \Delta t. \quad (3.26)$$

In this case, we only have to replace the $\psi_1(t - \tau)$ term with the ψ_1 term with l steps before the current i^{th} time step. Thus:

$$\text{if } l \in \mathbb{N}^+.$$

$$\mathbf{f} = \begin{bmatrix} \psi_2 \\ \omega_n^2 \varphi \psi_{1,i-l} - \omega_n^2 x_{st} - 2\zeta \omega_n \psi_2 - (\omega_n^2 + \omega_n^2 \varphi) \psi_1 \end{bmatrix}. \quad (3.27)$$

However, if this l is not a whole number, then we can approximately obtain this delayed term through interpolation between the two adjacent known values at different time instances. Although linear interpolation is just an approximation for $\psi_1(t - \tau)$, with a sufficiently small Δt time step, the error is negligible, however, it might increase the error rate of the Runge-Kutta method. In this case, let this delayed term be denoted as $\psi_{1,\tau}$

$$\text{if } l \in \mathbb{R}^+,$$

$$\mathbf{f} = \begin{bmatrix} \psi_2 \\ \omega_n^2 \varphi \psi_{1,\tau} - \omega_n^2 x_{st} - 2\zeta \omega_n \psi_2 - (\omega_n^2 + \omega_n^2 \varphi) \psi_1 \end{bmatrix}. \quad (3.28)$$

For the linear interpolation, we need to find the two adjacent time value, for this τ . Let a and b be the neighbouring indices of this intermediate time-delayed term

$$t_{i-b} < t_{i-\tau} < t_{i-a} \quad (a, b) \in \mathbb{N}^+, \quad (3.29)$$

$$t_i - b \cdot \Delta t < t_i - l \cdot \Delta t < t_i - a \cdot \Delta t. \quad (3.30)$$

Which simplifies to

$$a < l < b, \quad (3.31)$$

where we choose a and b to be whole numbers:

$$a = \left\lfloor \frac{\tau}{\Delta t} \right\rfloor, \quad (3.32)$$

$$b = \left\lceil \frac{\tau}{\Delta t} \right\rceil. \quad (3.33)$$

So the linear interpolation for the time delayed term in between adjacent know values, looks like the following

$$\psi_{1,\tau} = \frac{l-a}{b-a} (\psi_{1,i-b} - \psi_{1,i-a}) + \psi_{1,i-a}. \quad (3.34)$$

Now that we are familiar with the formulation using the Runge-Kutta method and have addressed the time delay component on how to handle it, we only need to select the appropriate time discretization Δt and the simulation length T . For constant spindle speed we choose this simulation length to be the period of the spindle which is τ . This means we are simulating one full revolution of the spindle. In order to make the simulation reflect reality and avoid convergence problems, we set the time step based on the shortest period present in the system. The common value in practice for Δt is a number lower than the $\frac{1}{20}$ -th of this period. In the case of a constant spindle speed, there are two periods present T_Ω and T_n , where

$$T_\Omega = \frac{2\pi}{\Omega} \quad T_n = \frac{2\pi}{\omega_n}. \quad (3.35)$$

So the time step depends on both of these periods

$$\Delta t \leq \frac{1}{20} \min(T_\Omega, T_n). \quad (3.36)$$

Summarizing the theory introduced in the previous chapter combined with the numerical solver detailed above, the stability analysis for a given Ω and w pair starts by taking a random \mathbf{S}_0 matrix with a size of $2n \times N_s$ that has the states of the initial conditions (n conditions for position and n for velocity so a total amount of $2n$ conditions).

$$\mathbf{S}_0 = \begin{bmatrix} S_{01,1} & S_{01,2} & \cdots & S_{01,N_s} \\ \vdots & \vdots & \ddots & \vdots \\ S_{02n,1} & S_{02n,2} & \cdots & S_{02n,N_s} \end{bmatrix}. \quad (3.37)$$

Then, using our numerical solver, we produce the solution of the equation of motion for the given initial conditions given by the columns of matrix \mathbf{S}_0 , whose solutions are placed in the corresponding column in matrix \mathbf{V}_0

$$\mathbf{V}_0 = \begin{bmatrix} V_{01,1} & V_{01,2} & \cdots & V_{01,N_s} \\ \vdots & \vdots & \ddots & \vdots \\ V_{02n,1} & V_{02n,2} & \cdots & V_{02n,N_s} \end{bmatrix}. \quad (3.38)$$

Then the \mathbf{H}_0 matrix can be determined by the following procedure

$$\mathbf{H}_0 = (\mathbf{S}_0^T \mathbf{S}_0)^{-1} \mathbf{S}_0^T \mathbf{V}_0. \quad (3.39)$$

And a new set of \mathbf{S}_1 matrix can be calculated

$$\mathbf{S}_1 = \mathbf{V}_0 \mathbf{A}_0 \boldsymbol{\mu}_0^{-1}. \quad (3.40)$$

Iterating through this procedure, commencing from the step as described after Eq. (3.37) but this time with the updated matrix of \mathbf{S}_1 , after an adequate number of iterations n_{iter} , the total count of Runge-Kutta runs performed n_{RK} , which is the most computationally demanding part in the iteration process, amounts to

$$n_{RK} = n_{iter} \cdot N_s. \quad (3.41)$$

Comparing this method to calculating the whole Φ matrix with a size of $2n \times 2n$ the necessary count of Runge-Kutta runs is expressed as

$$n_{RK} = 2n. \quad (3.42)$$

So as long as we adhere the following condition

$$n_{iter} \cdot N_s < 2n. \quad (3.43)$$

we can reduce the computational time, although this comes at the cost of accuracy. With the preliminary parameters seen in Tab. 2.1, a step size of $\Delta t = \frac{T_n}{25}$ the following stability maps had been created with a resolution of 100×100 , with the iteration parameters of $n_{iter} = 7$ and $N_s = 7$. The range was limited to 1700 – 2500 RPM.

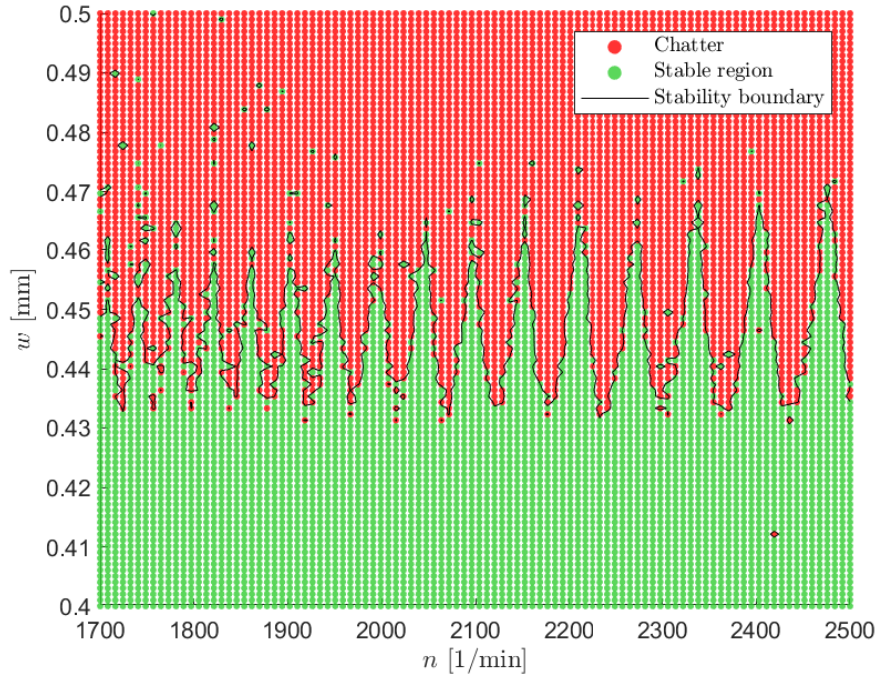


Figure 3.2: Stability map with ISIM

Taking the point with a spindle speed of 2000 RPM the size of the Φ matrix is

$$2n = 1998. \quad (3.44)$$

So with the chosen n_{iter} and N_s number the amount of Runge-Kutta runs at this point is

$$n_{iter} \cdot N_s = 49, \quad (3.45)$$

which is significantly less than the 1998 to be calculated with the semi-discretization method.

The effect of the subspace size and the number of iterations used was analyzed as shown in Fig. 3.3 with a resolution of a 150×150 grid.

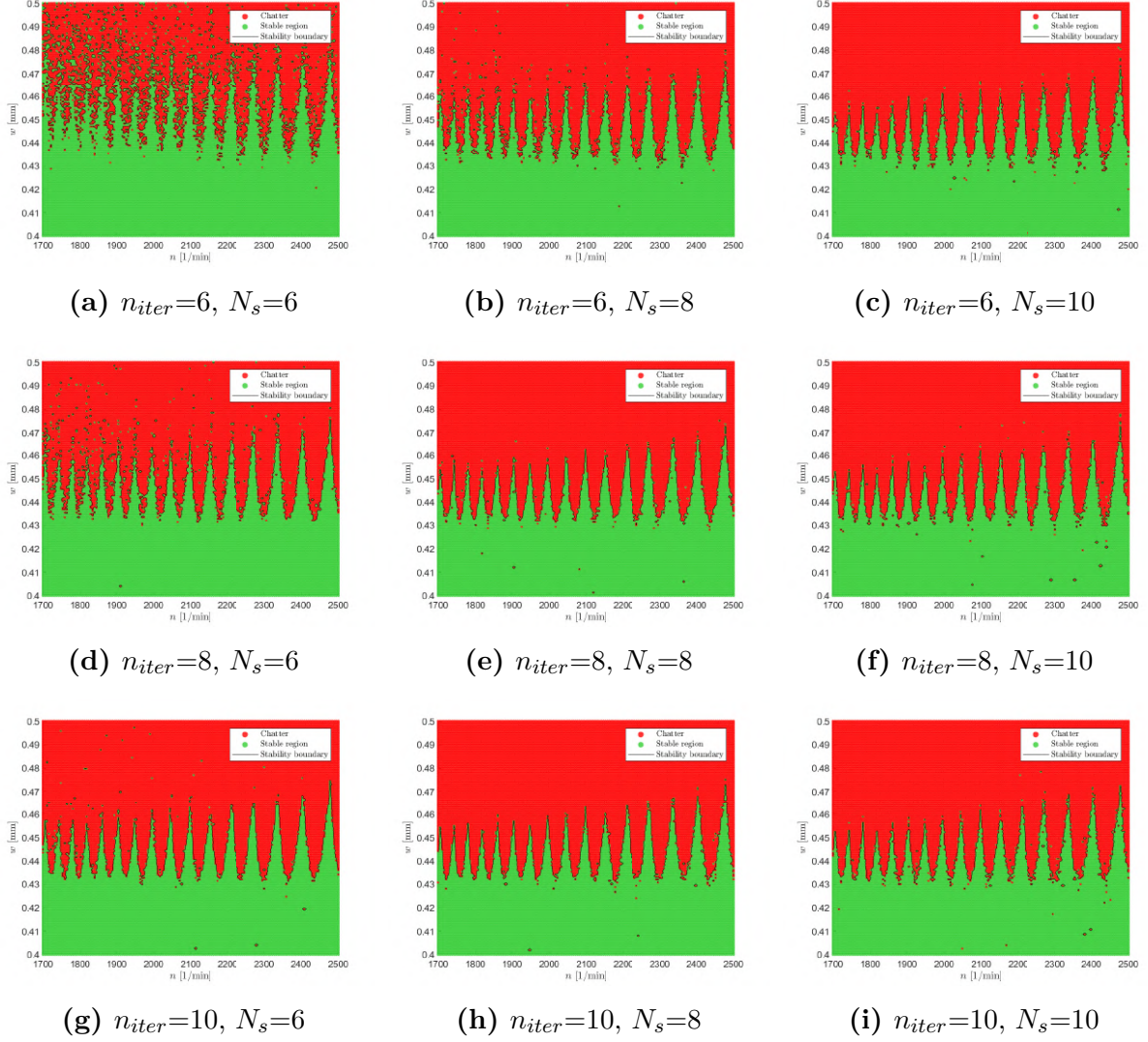


Figure 3.3: Impact of iteration and subspace size on stability maps

It is clearly visible that the applied methods proved the stability lobe structure well enough with a significantly small computational cost. However, due to some numerical problems some small noise can be found even for the Fig. 3.3 (i) panel, but it can be easily disregarded from the results.

3.3 Spindle speed variation

Among the several methods the researches have made to avoid chatter one of them is the Spindle Speed Variation (SSV). This method is used in various machining operations such as drilling, milling and especially in turning. As detailed in the previous sections earlier, the spindle speed plays a pivotal role in directly influencing the time delay, which is responsible for the regeneration of the cutting force and, thus, the occurrence of chatter during the machining process. By manipulating the spindle speed over time, the alignment of the cutting forces with the natural frequencies of the tool-workpiece system can be

prevented, and by doing the chatter vibration pattern can be disrupted. In an SSV operation, the shape of the function describing the spindle speed can vary, typically a triangle or a sinusoidal function. In our case, only sinusoidal will be used, so the rotational speed can be described as

$$n(t) \equiv n_0 + n_1 \sin\left(\frac{2\pi}{T}t\right). \quad (3.46)$$

From the equation above two basic parameters of the SSV [3] can be defined:

$$\text{RVF} \equiv \frac{60}{n_0 T} \quad (3.47)$$

$$\text{RVA} \equiv \frac{n_1}{n_0}. \quad (3.48)$$

Where the RVF number shows the ratio of the sinusoidal function period to the mean period τ_0 , and the RVA number shows the ratio of the sinusoidal function amplitude to the mean spindle speed n_0 . Expressing Eq. (3.46) in radians per second for later convenience we get

$$\Omega(t) = \Omega_0 + \Omega_1 \sin\left(\frac{2\pi}{T}t\right). \quad (3.49)$$

Also we would like to define this $\Omega(t)$ function in a way it ensures that during one sine wave of the spindle speed only complete amount of turns have been made by the spindle. To obtain this we should examine the change in the angular position of work piece between two times t_1 and t_2 , that can be calculated as

$$\Delta\varphi = 2\pi \int_{t_1}^{t_2} \Omega(t) dt. \quad (3.50)$$

With our function in Eq. (3.49) the integration can be expressed as

$$\Delta\varphi = \int_{t_1}^{t_2} \Omega_0 + \Omega_1 \sin\left(\frac{2\pi}{T}t\right) dt. \quad (3.51)$$

Where we set the integration limit to $t_1 = 0$ and $t_2 = k\tau_0$, meaning we are integrating through k mean period:

$$k2\pi = \int_0^{k\tau_0} \Omega_0 + \Omega_1 \sin\left(\frac{2\pi}{T}t\right) dt, \quad k \in \mathbb{N}^+. \quad (3.52)$$

By solving the integral and rearranging the equation we get

$$\frac{T}{\tau_0} = k, \quad k \in \mathbb{N}^+, \quad (3.53)$$

so by taking the value of T as a multiple of the k^{th} value of τ_0 , we can achieve complete sinusoidal wave within k rotations of the spindle. Expressing this condition with our base parameter RVF and k :

$$\text{RVF} = \frac{1}{k}, \quad (3.54)$$

this parameter can be easily adjusted to any desired value of k .

The adjustments to the Runge-Kutta method must begin with by computing the time delay for each discrete time in the simulation. Subsequently, we can directly use this τ value and substitute it into Eq. (3.34) at each timestep. This approach guarantees that for any given τ value a solution can be obtained through linear interpolation. An other modification that must be mentioned is the simulation length. Note that we assume that the feed rate is also varied; thus, h_0 is kept constant, however, later in the test, the feed velocity was constant. We consider its effect to be negligible. In the following figure the effect of the SSV implementation can be seen, as it shifts the lobes higher and increasing the stable region. In the following figure (Fig. 3.4) the RVF value was set to a constant 0.2 for each simulation while the RVA value was increased from 0.02-0.06 with a step size of 0.01.

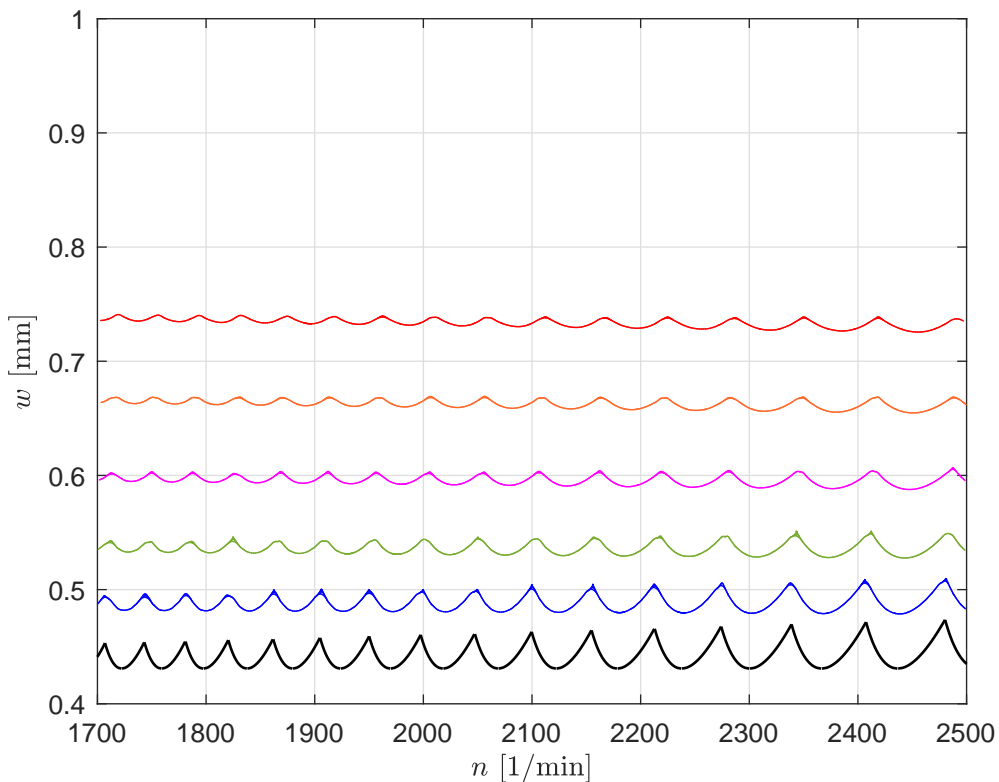
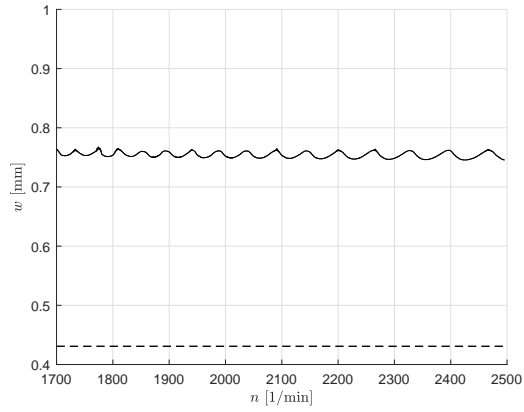


Figure 3.4: Effect of SSV implementation on stability lobes compared to the CSS turning (black). With an RVF value of 0.2. Above the black line, the associated RVA values are: 0.02, 0.03, 0.04, 0.05, 0.06.

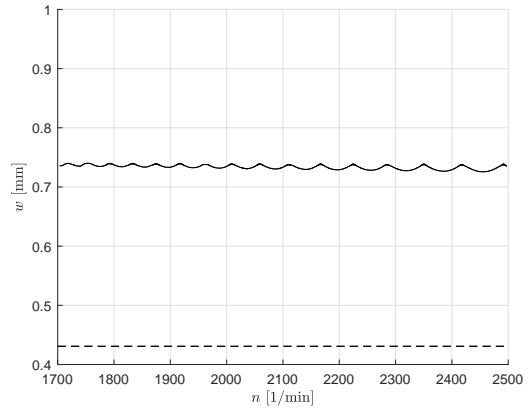
3.4 Spindle speed function optimization

In preparation for the stability testing through measurement, we conducted experiments involving various RVA and RVF values by using the MDBM combined with the ISIM, this way reducing the computational time even more. An important factor was that with the frequency inverter we used, we could only operate the machine in limited ranges. Therefore, we cannot set the RVF value too high, nor can we use a large RVA value.

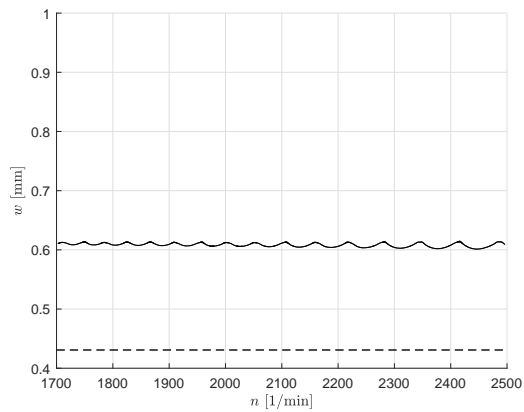
The following figure shows the effect of the RVA and RVF parameters on the stability lobes.



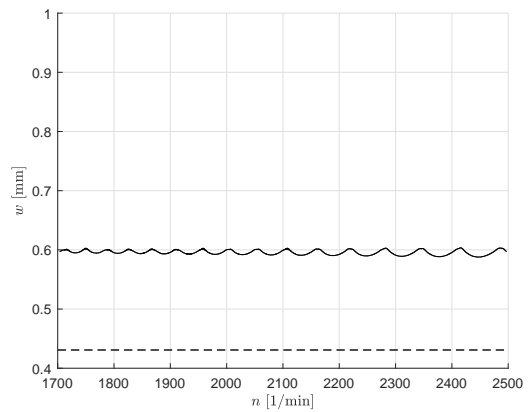
(a) $RVA=0.06$, $RVF=0.25$



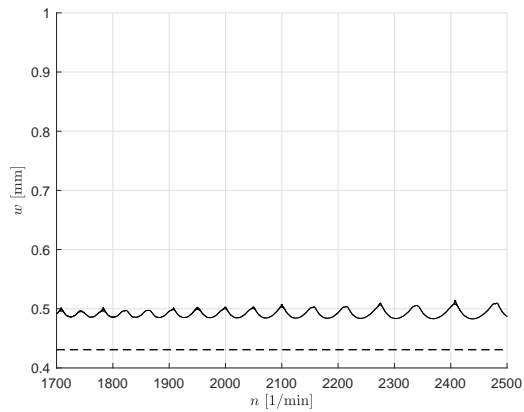
(b) $RVA=0.06$, $RVF=0.2$



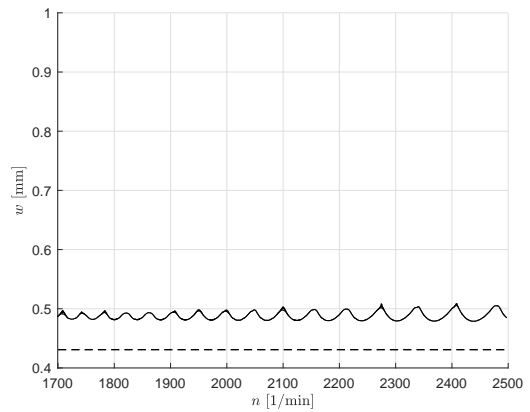
(c) $RVA=0.04$, $RVF=0.25$



(d) $RVA=0.04$, $RVF=0.2$



(e) $RVA=0.02$, $RVF=0.25$



(f) $RVA=0.02$, $RVF=0.2$

Figure 3.5: Impact of RVA and RVF parameters on the stability map. With the black dashed line representing the lower boundary of the CSS lobes and the black continuous line representing the SSV lobes

4 Stability testing with measurements

4.1 Cutting force characteristic

It was necessary to determine the forces acting on the tool tip that occur at different depths of cut and chip thickness during the machining. Understanding this so-called force characteristic of the tool is essential for determining the stability maps, as it establishes the connection between the depth of cut and the constantly changing chip thickness caused by the vibrating tool and the excitation force. This force characteristic is often described as a function $F_c(w, h)$ with coefficients called 'cutting coefficients', that must be determined by measurements. The type of this curve is not generally specified but needs to be empirically selected to best fit the measurement points.

4.1.1 Measurement

To carry out the measurement, the following approach was implemented. We placed and secured the lathe machine onto the table of the NCT milling machining with clamping elements. Then we measured the deviation of the lathe's axis from the global x -axis of the NC machine with the help of a laser distance meter. We then fine-tuned the lathe's position until the deviation became sufficiently small.

After positioning the lathe on the table, we attached the Kistler dynamometer device upside down next to the spindle of the NC machine, then we mounted the tool holder on the dynamometer directly with the tool attached to it. With this measurement setup, we were able to monitor the forces, while it was possible to examine various feed rates by moving the table in the negative x -direction and set the desired depth of cut by positioning the tool in the z -direction. The nominal rotational speed of the workpiece was set to $n = 1700$ RPM, also it was monitored during the measurements, with a reflective sensor mounted above the lathe chuck. The sensor were developed and used in [8]. The schematic model of this measurement setup can be seen on Fig. 4.1 .

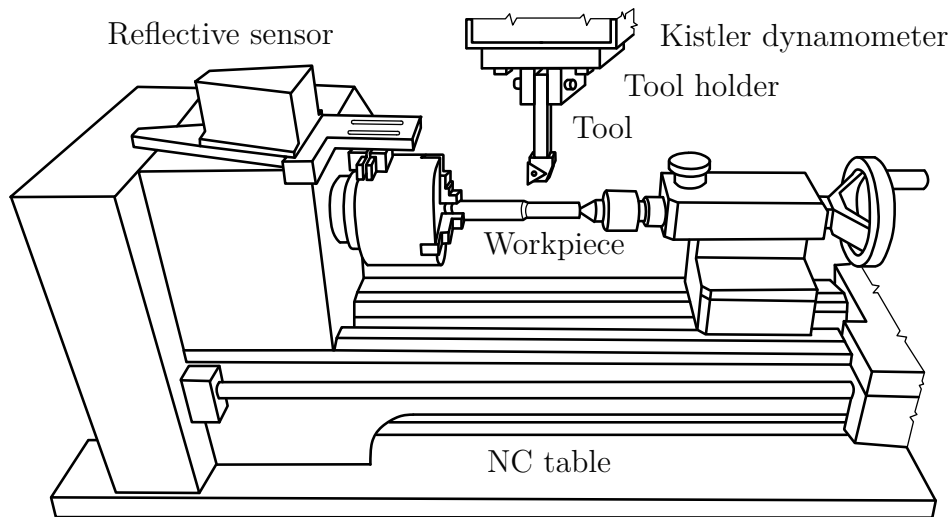


Figure 4.1: Measurement setup for force characteristic analysis

With the list of the used tools below and the technical data seen in Tab. 4.2, Tab. 4.1 and 4.3.

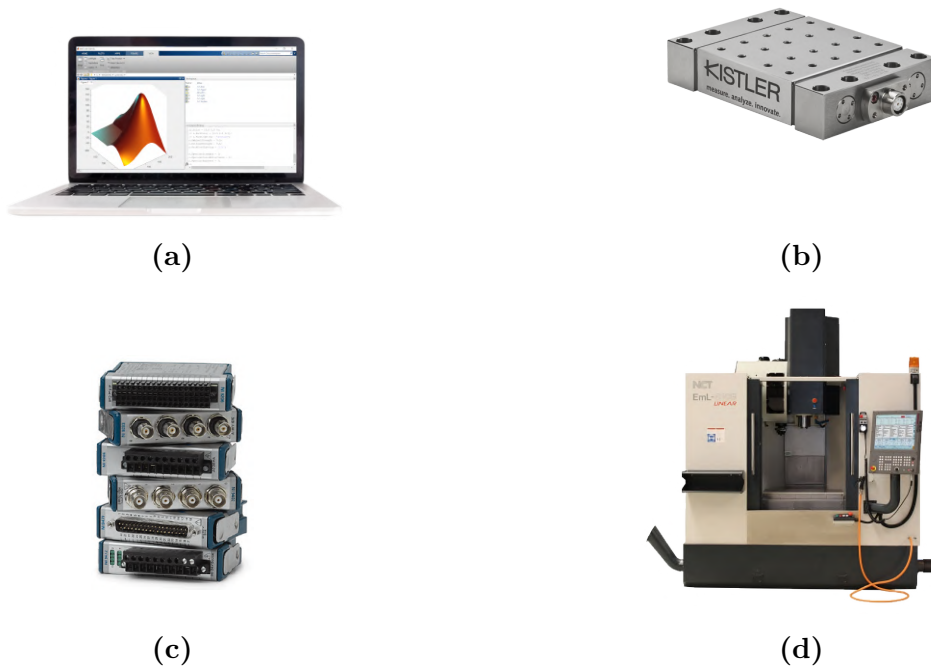


Figure 4.2: Tools of force characteristic measurement

(a) Processing module, (b) Kistler dynamometer, (c) NI DAQ module, (d) NCT machining center

National Instruments 9234 data acquisition module	
Signal range	-5 - +5 V
Number of input channels	4 pcs
maximum sampling frequency	51.2 Hz
Operating temperature	-40 - +70 °C

Table 4.1: National Instruments 9234 data acquisition module technical data

NCT EMR-610MS 3-axis CNC machining center	
Workspace	
Table size	800x450 mm
Number x Size x Distance of T-slots	3x18x100 mm
Table load capacity	400 kg
Spindle nose to table distance	125 - 635 mm
Spindle axis to column distance	535 mm
Positioning accuracy	< 0.02 mm
Repeatability	< 0.008 mm
Axes	
X / Y / Z wire type and number	Linear 2 / 2 / 2
X / Y / Z carriage number	4/4/4
X stroke	610 mm
Y stroke	460 mm
Z stroke	510 mm
X / Y / Z axis max. rapid traverse speed	30 / 30 / 24 MPP
Maximum feed rate	10 MPP

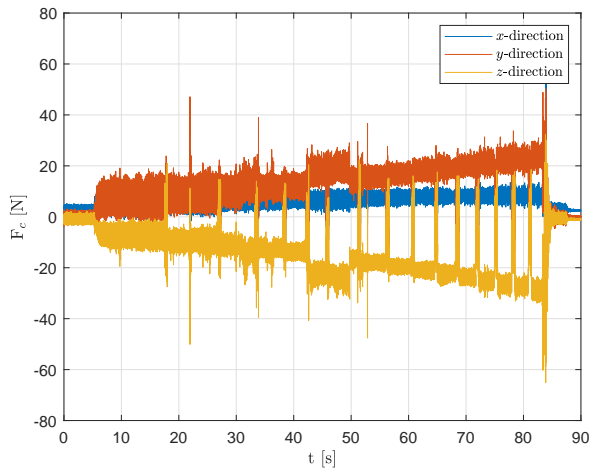
Table 4.2: NCT EMR-610MS 3-axis CNC machining center technical data

Kistler dynamometer

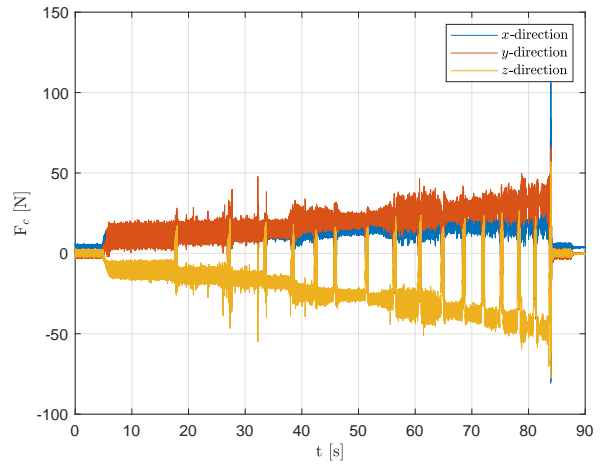
Type	9129AA
ID number	18007216
Manufacturer	Kistler
Maximum measuring range	10 kN
Measuring range	-10 - +10 kN
Measuring range F_x	-10 - +10 kN
Measuring range F_y	-10 - +10 kN
Measuring range M_x	-500 - +500 Nm
Measuring range M_y	-500 - +500 Nm
F_x sensitivity	-8 pC/N
F_y sensitivity	-4.1 pC/N
F_z sensitivity	-8 pC/N
Weight	3.2 kg
Operating temperature	0 - +70 °C
Natural frequency, $f_n(x)$	3.5 kHz
Natural frequency, $f_n(y)$	4.5 kHz
Natural frequency, $f_n(z)$	3.5 kHz

Table 4.3: Kistler dynamometer technical data

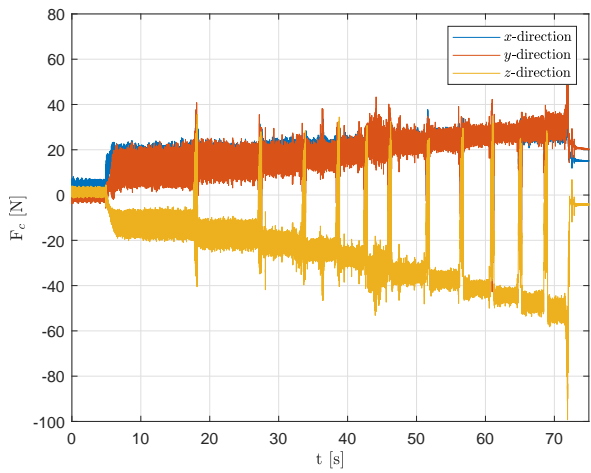
During the measurement, we first set a cutting depth, and then we divided the clamped workpiece into smaller sections in the x -direction, then we moved along these sections at different feed rates. We repeated this measurement with various cutting depths and adjusted the feed rate increments as necessary to achieve a better fit of the cutting force function. To perform these operations, we used G-codes which were input into the CNC machine. The following figures display the outcomes of the force measurement, that have been evaluated by a moving average in order to diminish noise and achieve a smoother signal.



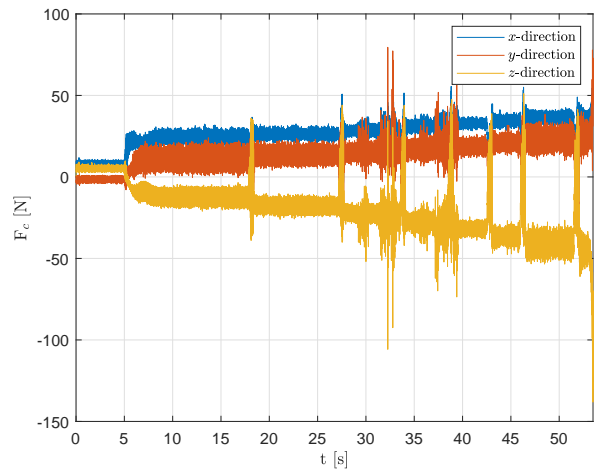
(a) $w=100$ [μm]



(b) $w=200$ [μm]



(c) $w=300$ [μm]



(d) $w=400$ [μm]

Figure 4.3: Force measurement signal with incrementally increasing feed rates from 10-160 μm with a step size of 10 μm . With the blue, red, yellow colors corresponding to the x , y , z directions in order.

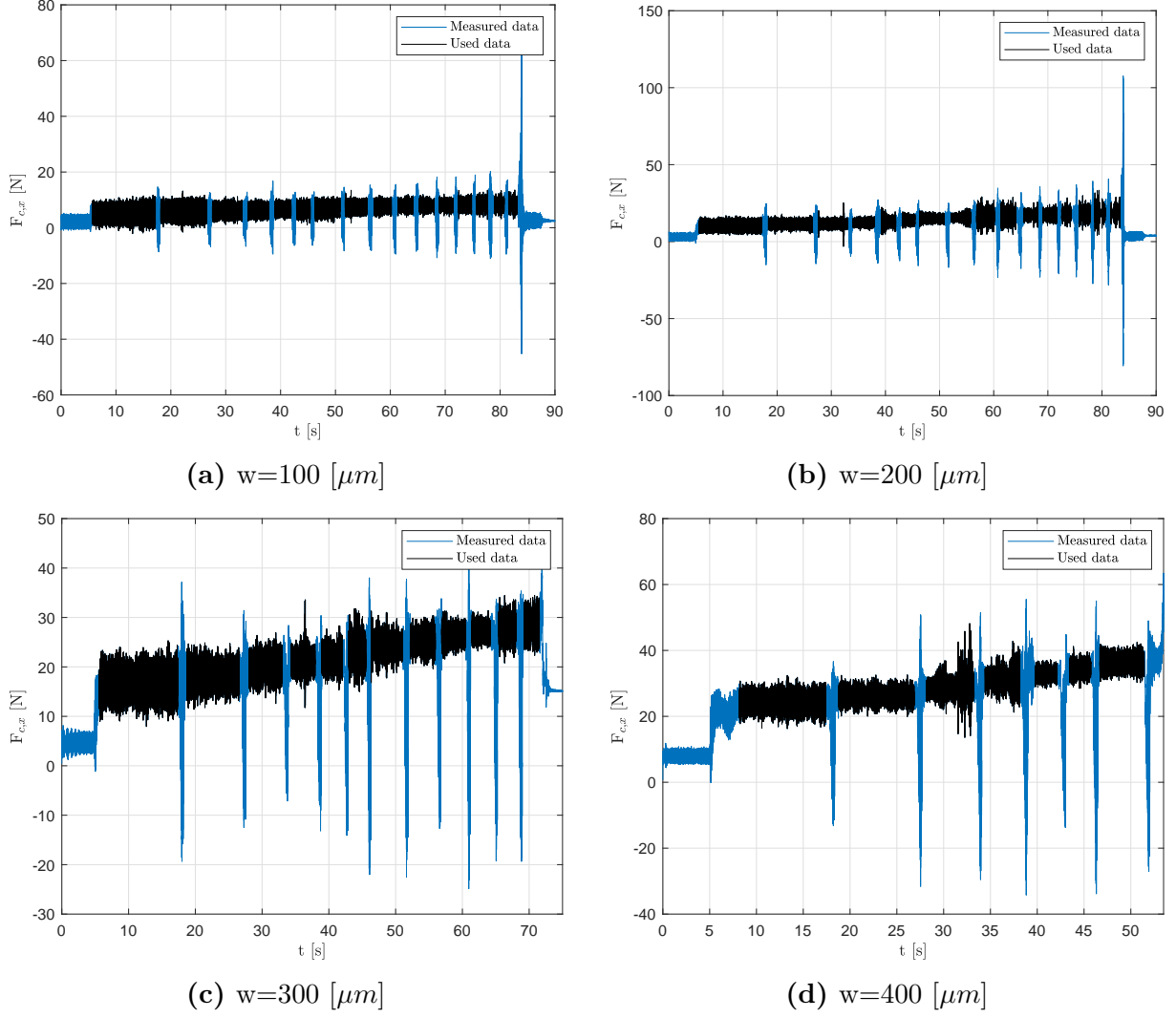


Figure 4.4: The measured raw data of the x component of the force (blue). The selected region for the cutting force fitting is denoted by black lines.

A 0.5 second pause in the feed was implemented between every feed rate changes in order to distinctly separate the data corresponding to different feed rates on the curves. These values were averaged for each feed rate and was compensated with the static noise of the force sensor, which is observable at the beginning and at the end of each measurement. The desired feed rate for a given nominal chip thickness was calculated according to the following equation

$$F = h \cdot n. \quad (4.1)$$

Where the chip thickness was set to a value of 10-160 μm with an increment of 10 μm . By visualizing the cutting force in 3 dimensions as a function of the chip thickness and the chip width, the cutting force can be estimated for any values of h and w through arbitrary surface fitting of $F_c(h, w)$. Based on the arrangement of the measurement points, the selected force characteristic is a shifted linear characteristics both in w and h , with the

coefficients of F_0 , K_0 and K_1

$$F_c(h, w) = F_0 + K_1 w(K_0 + h). \quad (4.2)$$

Subsequently we applied the least square method and fitted the aforementioned surface to the measurement points, only selecting those with a h value below $80 \mu m$, because we are only interested in the 0-80 μm region. The coefficient of determination was $R^2 = 0.9944$, which is close to the optimal value of 1. Therefore the fit is considered acceptable, and we find the fitted coefficients reliable for further calculations.

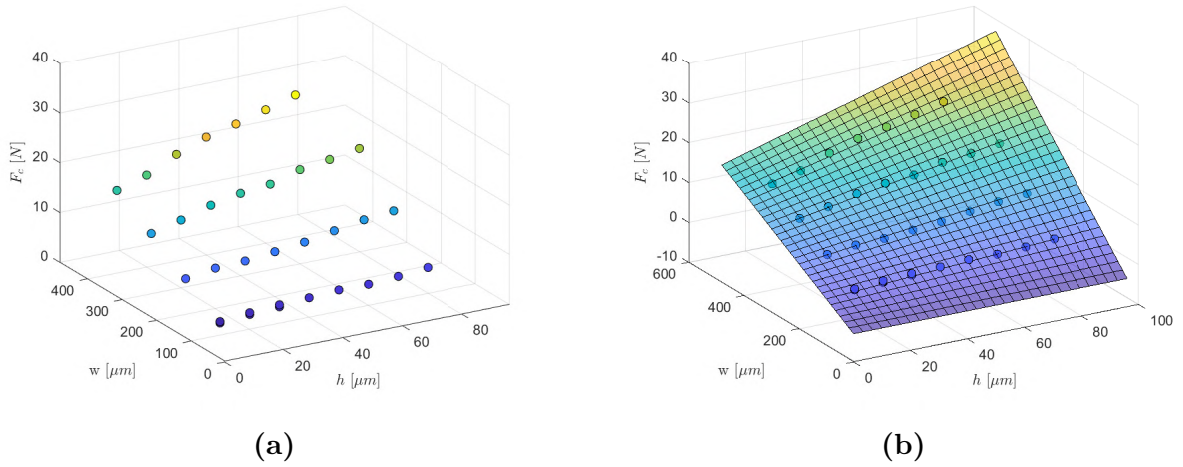


Figure 4.5: Force characteristic measurement data (a) measured points, (b) fitted surface

Thus the force characteristic with the calculated coefficients is

$$F_c(h, w) = -2.9235 + 431.25w(0.108 + h). \quad (4.3)$$

Where w and h are measured in millimeters, and F_c stands for force in Newtons and the coefficients are:

$$\begin{aligned} F_0 &= -2.9235 \text{ N}, \\ K_0 &= 0.108 \text{ mm}, \\ K_1 &= 431.25 \text{ MPa}. \end{aligned}$$

4.2 Dynamic properties of the system

Understanding the dynamic properties of the system is crucial for both analytical and numerical stability testing, as these require the system's modal parameters such as the natural frequency, relative damping ratio and the stiffness of the tool. These parameters can be determined utilizing the modern methods of modal analysis, specifically the Fast Fourier Transform (FFT). This method is widely used in music, science, mathematics and specifically in engineering applications as it revolutionized signal processing and analysis in the mid-20th century by Cooley and Tukey. The foundational concept of the FFT is the Discrete Fourier Transform (DFT) that converts a signal from its original domain to the frequency domain and vice versa, enabling analysis based on the frequency components of a system. However the computational complexity of the DFT limited its application for real-time implementations. By advancing from the DFT to the FFT the computational time was drastically reduced. With the help of the FFT we were able to generate the Frequency Response Function (FRF) of the tool detailed in the next subchapter.

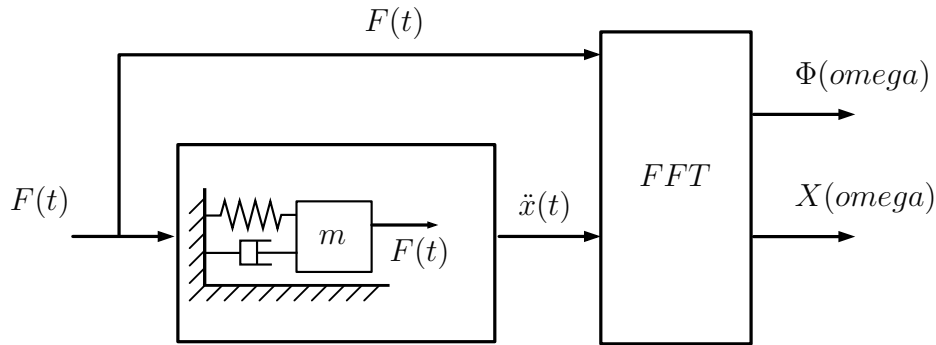


Figure 4.6: Schematic sketch of modal analysis

4.2.1 Measurement

The following setup was used in order to determine the dynamic properties. A piezoelectric accelerometer was attached on the edge of the tool and connected to a *National Instruments* Data Acquisition (DAQ) device. The excitation was performed using a modal hammer, which was also connected to the DAQ. Then the DAQ was connected to the computer which was the processing module where the analysis was done in *MATLAB* environment.

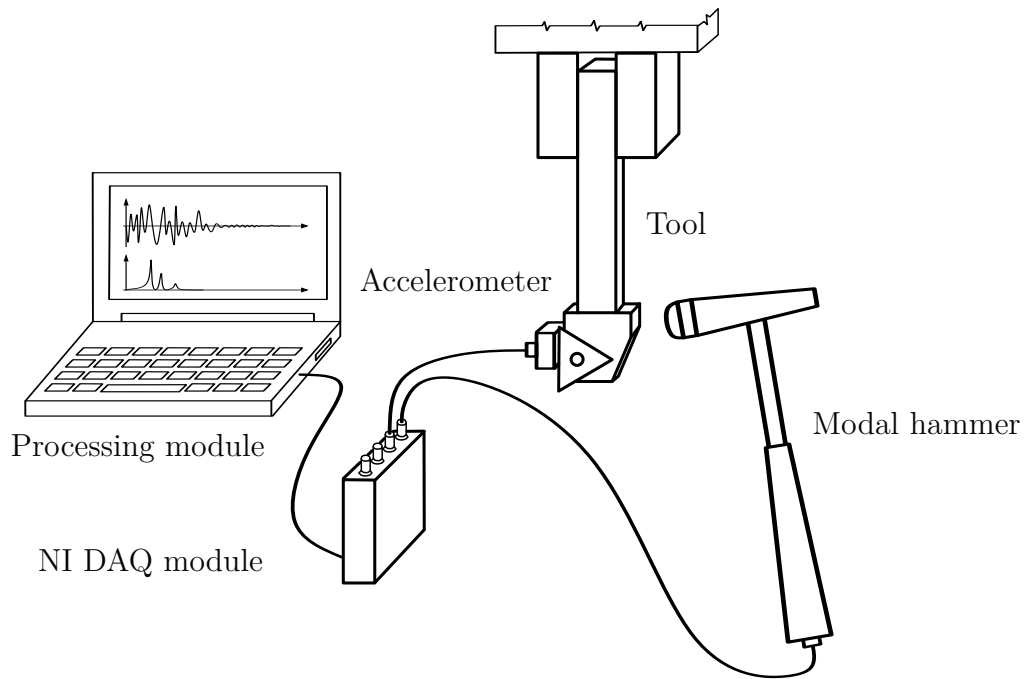


Figure 4.7: Measurement setup of modal analysis

At the initial setup we clamped the tool into the tool holder, which was directly positioned to the Kistler dynamometer (Fig. 4.8a). However with this setup, the system proved to be overly rigid therefore no successful stability analysis could be performed. For this reason we changed the original setup and in between the tool and the dynamometer we inserted a more compliant tool holder element (Fig. 4.8b). This allowed us to operate within a more favorable stiffness/damping range which resulted in successful stability testing detailed in Chapter 4.3. The following results will only include the measurements done using the new setup.



Figure 4.8: (a) Initial setup with the tool directly positioned on the Kistler, (b) new setup with a compliant tool holder inserted in between the tool and the Kistler

The measurement tools that were used can be seen in the following figures, with their

technical data in 4.5, 4.4 and 4.1.

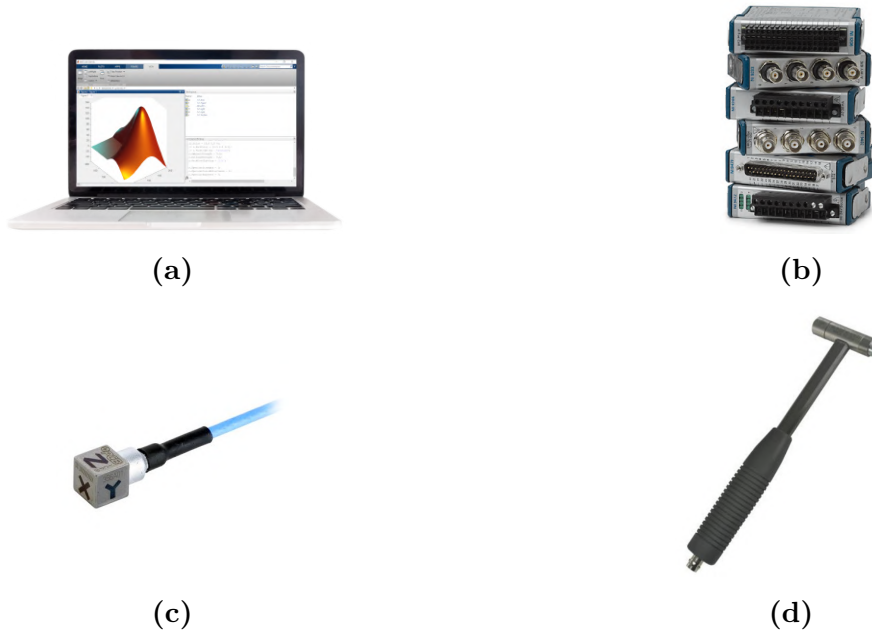


Figure 4.9: Tools of modal analysis

(a) Processing module, (b) NI DAQ modul, (c) accelerometer, (d) modal hammer

PCB Modally Tuned ICP Impact Hammer	
Sensitivity ($\pm 15\%$)	2.25 mV/N
Measurement range	± 2224 N
Resonant frequency	≥ 22 kHz
Nonlinearity	$\leq 1\%$
Excitation voltage	20-30 VDC

Table 4.4: PCB Impact Hammer data

Miniature Triaxial ICP Accelerometer technical data	
Sensitivity ($\pm 20\%$)	5 mV/g
Measurement range	± 1000 g pK
Resonant frequency	≥ 50 kHz
Nonlinearity	$\leq 1\%$
Excitation voltage	28-30 VDC

Table 4.5: PCB accelerometer technical data

During the excitation, we aimed to provide an impulse-like excitation as much as possible, while we observed the acceleration signal of the accelerometer and the force signal of the hammer. After applying the FFT on the measured time signal, we were able to

generate the Frequency Response Function (FRF) of the tool, which will be noted as $H_{i,j}^{acc}$, with the indices i referring to measuring in the i -direction and j referring to exciting in j -direction, and acc meaning the transfer function is an acceleration function

$$H_{i,j}^{acc}(i\omega) = \frac{A_i(i\omega)}{\Phi_j(i\omega)} \quad (4.4)$$

with A_i being the transformed acceleration signal and Φ_j being the transformed force signal. In In Fig. 4.10 we can see the acceleration functions of different excitation and measurement directions where the rows of the subfigures displacements corresponds to the different measurement directions (x,y,z) while the columns corresponds to various excitation directions.

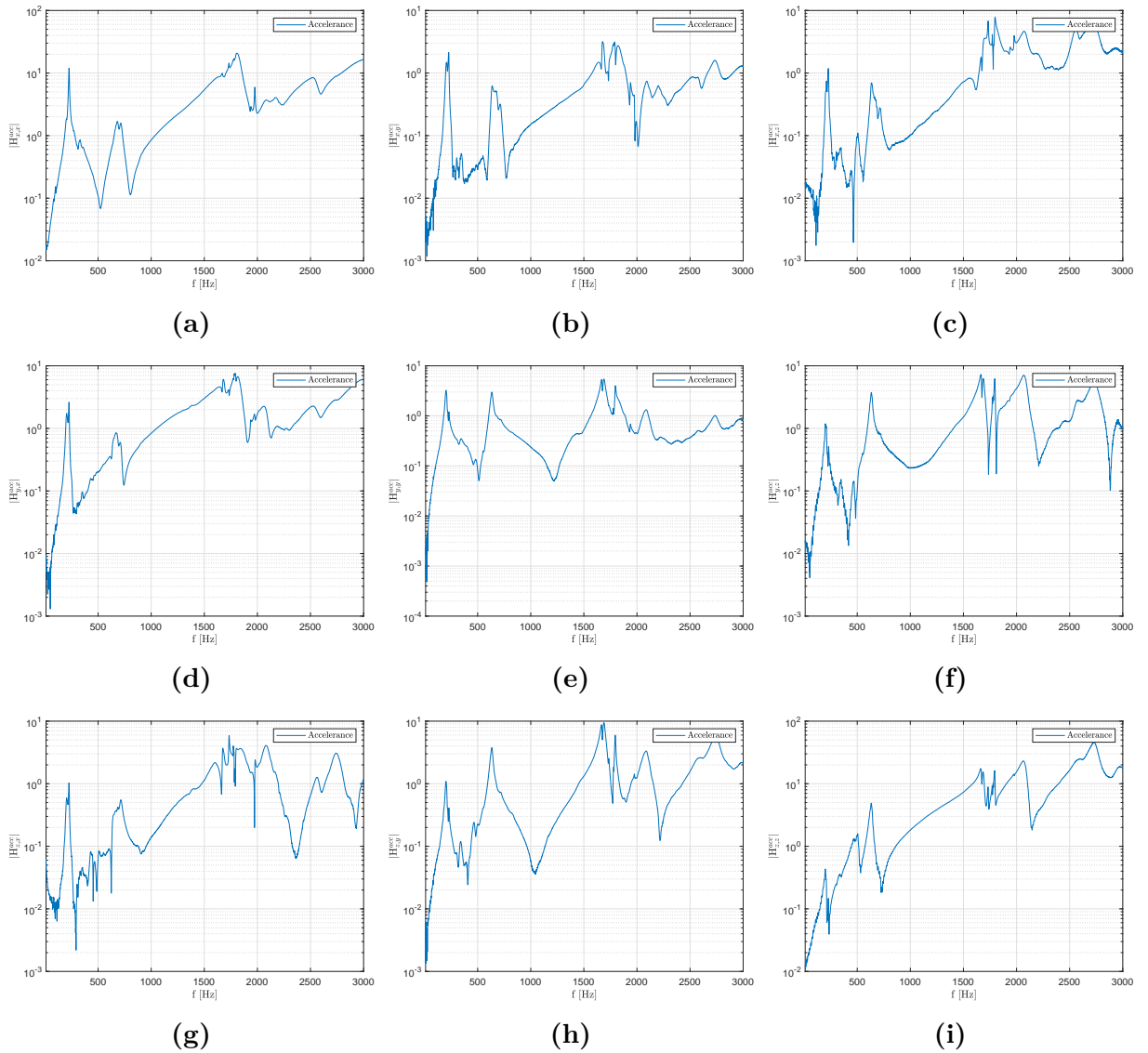


Figure 4.10: Accelerance functions of different measurement and excitation directions

Since we are using a 1 DoF model, we specifically focusing on the x -directional response for an x -directional excitation, the relevant figure required is Fig. 4.10a. The 1 DoF

approximation is supported by the fact that the FRF in the $x-x$ is at least 5 times larger than in any other components. From the positions of the peaks of the accelerance function, the natural frequencies can be determined, and from the height of these peaks, the most dominant natural frequencies can be identified. The mobility and receptance functions can be easily calculated from the accelerance functions as these originate from the FFT of the velocity and position of the tool and as we seen in Eq. (2.42) an integration in time domain turns into a division in the frequency domain so:

$$\text{Accelerance} \xrightarrow{\cdot \frac{1}{i\omega}} \text{Mobility} \xrightarrow{\cdot \frac{1}{i\omega}} \text{Receptance}. \quad (4.5)$$

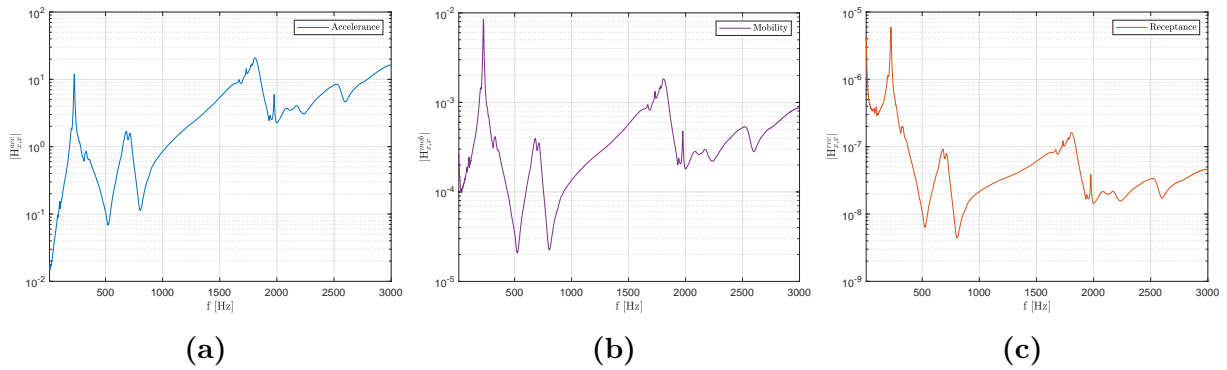


Figure 4.11: $|H_{x,x}|$ (a) accelerance, (b) mobility, (c) receptance functions

By fitting a 1 DoF model to the first dominant peak on the receptance plot, we were able to determine the modal parameters of the system. The shape of the fitted curve we are using is similar to the resonance curve, but it requires a division with the stiffness

$$f(f_n, \zeta, k) = \frac{1}{k} \frac{1}{\sqrt{\left(1 - \left(\frac{f}{f_n}\right)^2\right)^2 + 4\zeta^2 \left(\frac{f}{f_n}\right)^2}} \quad (4.6)$$

Then applying the fit (Fig. 4.12) to the generated receptance curve with a coefficient of determination of $R^2 = 0.9794$ the fit is considered acceptable and the modal parameters can be seen in Tab. 4.6.

Parameter	Value	Dimension
f_n	226.17	Hz
ζ	0.0142	1
m	2.9214	kg
k	$5.8995 \cdot 10^6$	N/m
c	40.4073	Ns/m

Table 4.6: Fitted and calculated modal parameters from the measured data

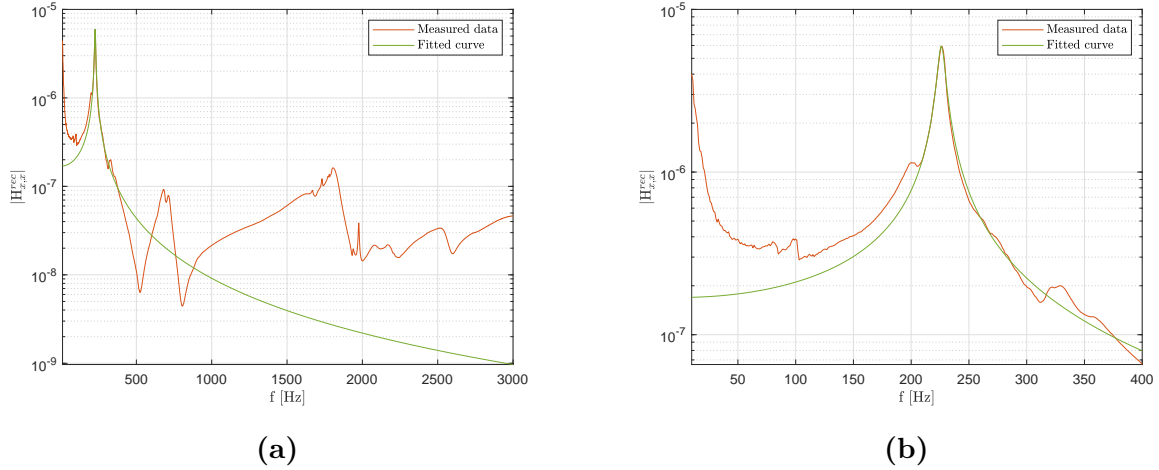


Figure 4.12: (a) Measured receptance plot in orange with fitted 1 DoF curve in green
 (b) zoomed view of fitted curve

The Real and Imaginary part of the measured and fitted curve can also be plotted and compared in the next figures.

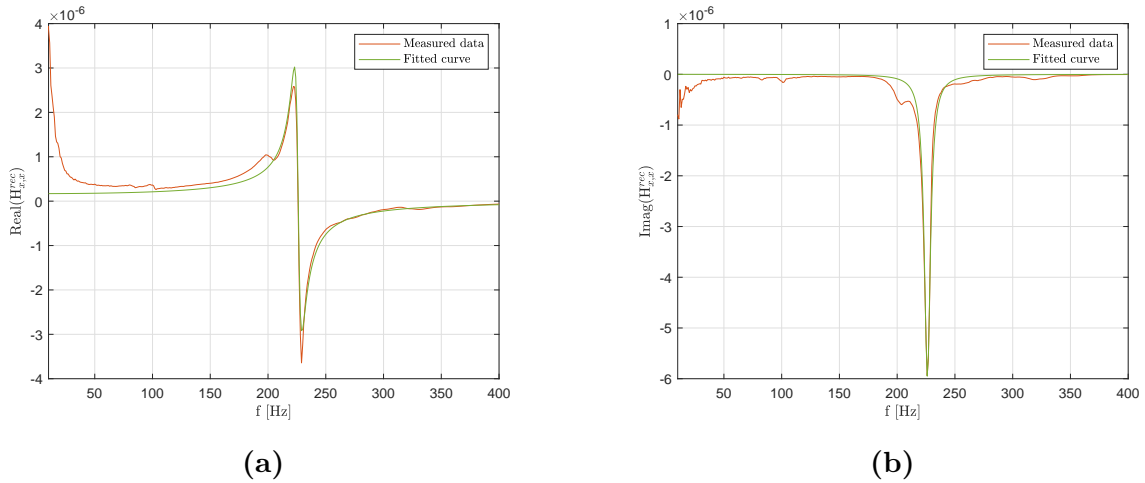


Figure 4.13: Measured (orange) and fitted (green) receptance functions. (a) Real part of receptance function, (b) imaginary part of receptance function

4.3 Stability testing

4.3.1 Measurement setup

The measurement setup necessary for stability testing was similar as seen in Chapter 4. Initially, we set a relatively small depth of cut and a $50 \mu m$ chip thickness, which we tried to maintain during the measurement by calculating the necessary feed rate based on the formula seen in Eq. (4.1). Each measurement was done on a approximately 10 mm long section on the workpiece. After the data collection we needed a method to determine

whether or not the tool lost its stability. To do this, we analyzed the spectrum of the measured force signal, where the peak amplitude corresponds to the chatter frequency of the tool. After a few test measurements, we established an amplitude level that we considered a stability threshold which was 20 m/s^2 .

4.3.2 Constant spindle speed

Starting the measurement with constant spindle speed turning the measured points can be compared to the analytical solution calculated by the directly measured FRF and by the fitted modal parameters, together with the fitted force coefficients. This comparison can be seen in Fig. 4.14. It is visible that the stability lobes do not cover the stable and unstable points determined by the measurement; the reason for this might lie in the inaccurate depiction of the force characteristic.

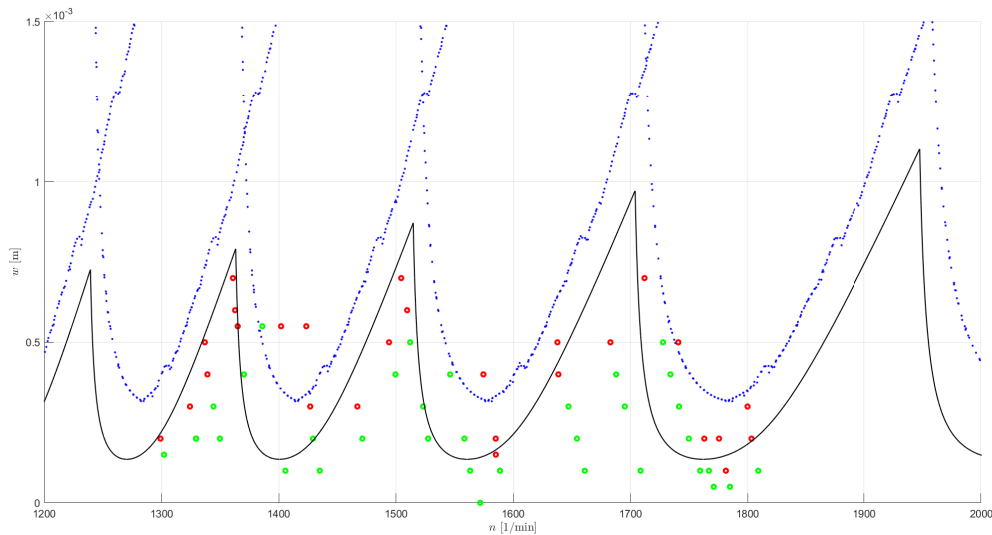


Figure 4.14: Comparison of analytical (black), D-separation method (blue) and measurement results with $K_1 = 431.25 \text{ MPa}$ cutting coefficient. Green and red scatters representing the stable and unstable turning.

We can see that the D-curve method approximately corresponds to the map calculated analytically. A possible reason for the shift of the D-curve solution from the analytical could be the use of a 1 DoF model and the imperfect fitting of the receptance function.

By tuning the force coefficients, more precisely the K_1 value which becomes apparent in the time-varying excitation force, we can align the curve to fit the measurement points best. The best fit was achieved at $K_1 = 1000 \text{ MPa}$.

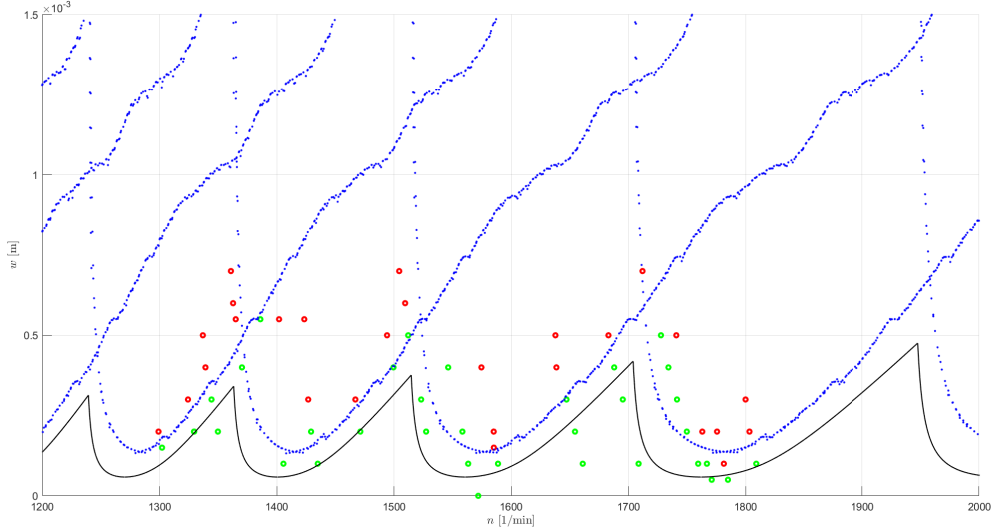


Figure 4.15: Comparison of analytical (black), D-separation method (blue) and measurement results with $K_1 = 1000$ MPa cutting coefficient. Green and red scatters representing the stable and unstable turning.

Note that the previous K_1 value was 431.25 MPa. Comparing this to the updated $K_1 = 1000$ MPa is a 232 % increase, which would require the reevaluation of the force characteristic parameters. The main reason behind this drastic difference could be a breakage of the tool at a certain stage during the force characteristic measurement, prompting a replacement of the lathe tool potentially changing the cutting coefficients. Furthermore, the orientation of the tool was also changed, which might have an influence too.

4.3.3 Periodic spindle speed (SSV)

We followed the measurement process by implementing the SSV, with the help of the frequency inverter [8]. We set the [RVF, RVA] values to [0.1, 0.08] and [0.2, 0.04], however, the spindle cannot hold the desired spindle speed due to its dynamics [8], thus the realized values are [0.0967, 0.0659] and [0.1912, 0.0285] as an average of the measured values. At these two selected SSV, we searched for the stability along the w parameter. In Fig. 4.16 and Fig. 4.17 the horizontal axis represents, the nominal spindle speed, while in the measurement points, the variation level is also represented by a horizontal line segment. In the first case (Fig. 4.16) with faster variation and smaller amplitude, we can find the significantly increased stability limit, which were well predicted by the measured cutting force model ($K_1 = 431.25$ MPa). There is a slight underestimation by the model. In the second case (Fig. 4.17), we could not find the stability limit. All the selected points were stable. We could not further increase the chip width due to the power limitation of the spindle. Still, if we assume a slight underestimation of the predicted stability by the model with $K_1 = 431.25$ MPa, then the measurements points confirms the increased predicted stability limit.

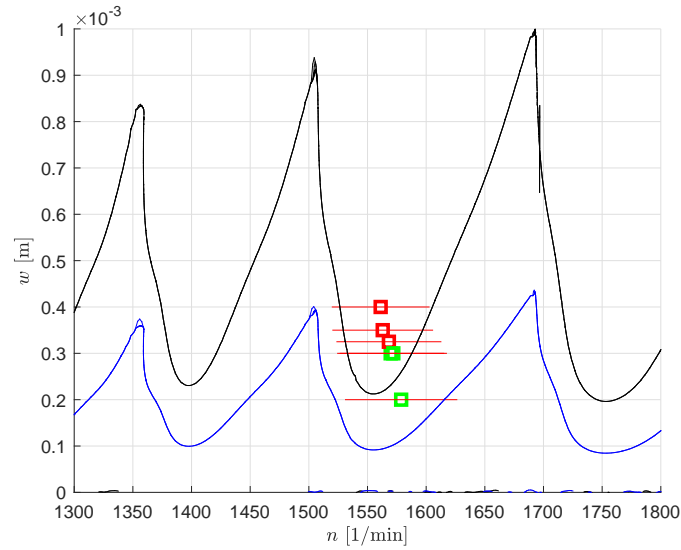


Figure 4.16: Stability map with the implementation of SSV. The numerical prediction based on the ISIM for $RVA = 0.04$, $RVF = 0.2$ and with force coefficient (blue) $K_1 = 1000$ MPa and (black) $K_1 = 431.25$ MPa

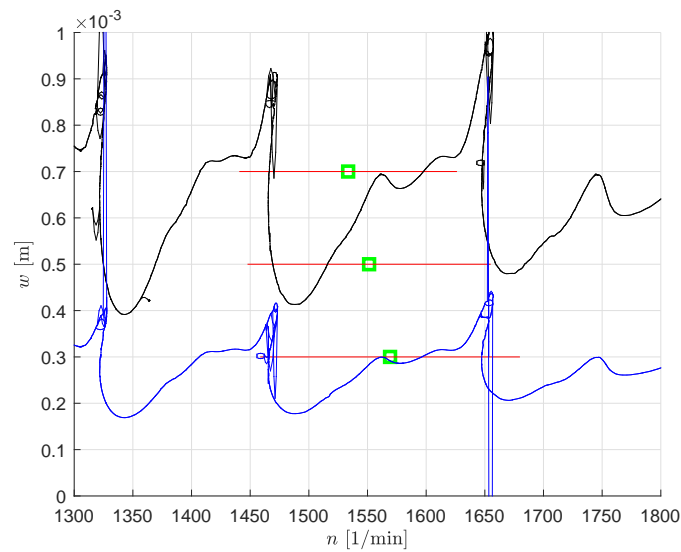


Figure 4.17: Stability map with the implementation of SSV. The numerical prediction based on the ISIM for $RVA = 0.08$, $RVF = 0.1$ and with force coefficient (blue) $K_1 = 1000$ MPa and (black) $K_1 = 431.25$ MPa

The applied SSV were really successful in increasing the stability limit. Even with only 10% of spindle speed variation, we could at least quadruple (0.7/0.15) the maximal achievable stable chip width at the selected spindle speed.

5 Summary

In the current work, we focused on mitigating the unwanted vibrations known as 'chatter' and providing a comprehensive analysis of stability with both constant and variable speed turning with a specific emphasis on varying the spindle speed periodically. This was a very complex task: mechanical and mathematical modelling were assisted with state-of-the-art numerical simulations for stability analysis in frequency and time domain. The results were confirmed by detailed measurements for which we had to create viable test equipment; we had to perform modal analysis and extract modal parameters. Finally, we confirmed the stability chart for CSS with high accuracy and also validated the stabilizing effect of the SSV.

As a first step, we conducted analytical stability testing, utilizing a 1-degree-of-freedom mechanical model and deriving it in both frequency and time domains. In frequency domain, we implemented the D-separation method based on the modal parameter and based on the measured FRF. In the time domain numerical stability testing, we employed the combination of two advanced methods, the semi-discretization method and the implicit subspace iteration method which based on direct simulation via RK4 method. These numerical methods were implemented for both constant and variable speed turning, allowing us to evaluate the efficiency of the spindle speed variation technique.

Moving on to the measurement side, we determined the force characteristic of the tool by creating a unique measurement environment by combining a lathe machine with the NCT machine available at the Department of Applied Mechanics at BME. We also assessed the dynamic properties of the system across multiple degrees of freedom using modern methods of modal analysis. This measurement confirmed that we made appropriate simplifications in our mechanical model, by setting up our 1-degree-of-freedom model in the most critical direction.

With another numerical method, the multi-dimensional bisection method, we were able to calculate the stability lobes of the tool directly from transfer functions computed from the transfer function measurement data. This method was used during the validation of constant spindle speed turning. The stability limit predicted based on the determined modal data and force characteristics provide a sufficient approximation of the measured stability limit. However, with a fitted simple linear force characteristic, we got an almost perfect match between the calculation and the measurements.

Subsequently, stability testing were performed turning with spindle speed variation and the results were compared with every stability testing methods. The prediction based on the ISIM, provides good estimation for the increase of the lower envelope of the stability limits.

Acknowledgement

This work was supported by the Hungarian Scientific Research Fund NKFI FK-138500 and by the MTA-BME Lendület Machine Tool Vibration Research Group. We thank Dávid Hajdu for support with the 1DoF test rig and the ready-to-use modal analyzing software.

References

- [1] G. Stépán. *Retarded Dynamical Systems: Stability and Characteristic functions*, volume 159. Longman, London co-published with Wiley, New York, 1989.
- [2] J. Munoa, X. Beudaert, Z. Dombovari, Y. Altintas, E. Budak, C. Brecher, and G. Stepan. Chatter suppression techniques in metal cutting. pages 785–808, 6 2016.
- [3] G. Urbikain, D. Olvera, LN. López de Lacalle, and A. Elías-Zúñiga. Spindle speed variation technique in turning operations: Modeling and real implementation. pages 384–396, 8 2016.
- [4] D. Bachrathy and G. Stépán. Bisection method in higher dimensions and the efficiency number. pages 81–86, 6 2012.
- [5] D. Bachrathy and G. Stépán. Improved prediction of stability lobes with extended multi frequency solution. pages 411–414, 2013.
- [6] T. Insperger and G. Stépán. Semi-discretization method for delayed systems. pages 503–518, 2002.
- [7] M Toth, D. Bachrathy, and G. Stepan. Effect of wavy tool path on the stability properties of milling by the implicit subspace iteration method. pages 1781–1789, 12 2016.
- [8] L. Pothárn. Változó fordulatszámú esztergálás vizsgálata. Technical report, Department of Applied Mechanics, Budapest University of Technology and Economics, June 2023.